Broadband Monolithic Constrained Lens Design

by

Leonard Thomas Hall

B.E. (Electrical & Electronic, with Honours),
The University of Adelaide, Australia, 2000

Thesis submitted for the degree of

Doctor of Philosophy

in

School of Electrical and Electronic Engineering,
Faculty of Engineering, Computer and Mathematical Sciences
The University of Adelaide, Australia

August, 2009

Chapter 7

Contributions to Lens Design and Construction

THIS chapter addresses the numerous practical challenges of monolithic constrained lens implementation using modern electromagnetic simulation software to explore the interface between the microstrip ports and the parallel plate transmission medium of the Rotman lens. By treating the ports independently, rather than as part of the Rotman lens system, the mechanisms that limit monolithic constrained lens performance are clarified. This permits a detailed discussion of the impact port properties have on Rotman lens design and construction.

The boundaries of realistic Rotman lens performance is clearly defined, and an effective method of impedance matching all ports is described. Port matching is extended to include fixed magnitude and phase coupled ports, and fixed magnitude and variable phase coupled ports. The chapter finally presents three lens examples, illustrating how the insight gained from this work has been applied to improve the performance of the Rotman lens.

7.1 The Port to Lens Interface

The discrepancy between the theoretical and practical performance, observed in Rotman lens implementation, is caused largely by the behaviour of the lens body to port intersection. An analysis of this intersection leads to a much improved understanding of the tradeoffs in constrained lens design.

The port structures are examined in the same way antenna elements are examined. First the two dimensional beam pattern of a single impedance matched element is characterised for a range of port geometry and size. The single element is then examined in the presence of other elements with a focus on mutual coupling and impedance.

The difficulty in characterising the microstrip or stripline junction is that measurements of a single port cannot be easily made independently of all other ports around the body of the lens. To characterise an isolated port interface, the port must be connected to a parallel plate region extending to infinity. In this way the port interface, rather than the termination of the parallel plate region, is responsible for all reflected power.

The port structure has been implemented as an electromagnetic model using HFSS as shown in Figure 7.1(a). The green line represents a non-reflecting boundary that effectively extends the parallel plate region to infinity. The black line shows the boundary of the upper conductor and the red line is the port excitation. The electromagnetic model has been designed to examine the effect of:

- wavelength or frequency,
- substrate dielectric constant,
- substrate height,
- width of the port junction,
- angle between port and infinite parallel plate region,
- angle of the infinite parallel plate region either side of the port,
- the cut off frequency of higher order modes, and
- coupling to adjacent ports.

This model is limited to characterising a single port at the edge of an infinite parallel plate region. To examine the effect of multiple ports the geometry shown in Figure 7.1(b)

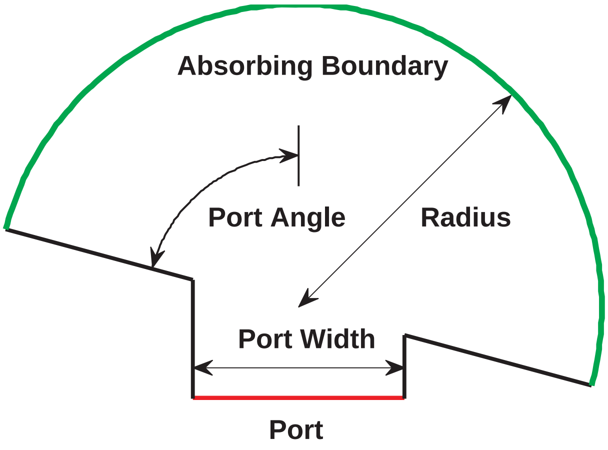

(a) Single port junction model

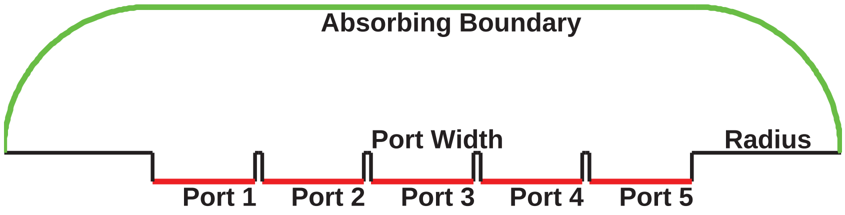

(b) Multi-port junction model

Fig. 7.1: Single and multiple port model. The performance of the single microstrip port is examined using these models. Subfigure (a) represents a port in isolation and Subfigure (b) represents a port in the presence of other ports. The green lines represent the non-reflecting boundary, the red lines are the port excitation and the black lines define the outer contour of the microstrip port. Parameters such as port angle and port width can be varied to determine the effect on input impedance and two dimensional beam pattern. The radius must be large enough to ensure the proximity of the boundary does not affect the results.

has been used. This model implements multiple ports along the boundary of the infinite parallel plate region, enabling mutual coupling and mutual impedance properties, of different port geometries, to be explored.

7.1.1 Port Beam Pattern

The electromagnetic model depicted in Figure 7.1(a) has been used to show that the port beam pattern behaviour closely resembles that predicted by the two dimensional aperture approximation, described in Section 4.3.1. The electromagnetic models have also been used to explore the effect of port parameters on the two dimensional beam pattern and the phase centre of a microstrip port. This is achieved using a microstrip port to excite a propagating wave within the virtual lens body. The magnitude of the E-field is calculated at a constant radius from the centre of the port. By examining the properties of this field, the beam pattern, and aberrations are predicted. Figure 7.2 shows the calculated two dimensional beam pattern for different choices of port width, dielectric constant, substrate height, port angle, and port sidewall geometry.

As predicted by two dimensional aperture theory, the port beam pattern is dominated by effective port width. In addition, Figure 7.2(a) shows the two dimensional aperture antenna pattern is truncated at ± 90° where the parallel plate region abruptly ends. As expected the beam becomes narrower and peak gain increases as the port width is increased. Frequency has a similar effect, as decreasing the guided wavelength increases the effective width of the port. Figure 7.2(b) shows the characteristic sinc function dependance at 20 GHz and effective port width of λ_g.

The substrate choice affects the beam pattern primarily through its affect on fringing fields. The affect of the dielectric constant on the port's two dimensional beam pattern is shown in Figure 7.2(c). The width of the port has been scaled to maintain a port width of $\lambda_g/2$. Lower dielectric values significantly reduce the fringing fields and therefore the effective width of the port. This results in a broader pattern and lower peak gain. The substrate height has a similar effect. As the height increases, the fringing fields become larger, increasing the effective port width and producing a more directional beam pattern. Figure 7.2(d) shows this clearly as the beam pattern becomes much narrower for substrate height of $\lambda_g/4$.

Section 4.3.3 explained that radiation from a port can be directed by adjusting the angle of the port. To examine the effectiveness of this approach, the model shown in Figure 7.1(a) has been arranged to vary the sidewall angles of the port to simulate a port incident on an angle. If the port's beam pattern remains centred on boresight the beam direction is independent of sidewall angle and the beam can be pointed with good control.

Figure 7.2(e) clearly shows that the beam pattern remains a close approximation to the 0° port. The most obvious difference is the change in angle where the beam pattern is truncated due to the edge of the parallel plate region. Less obvious is the small beam offset and slight increase in gain. Figure 7.2(f) appears as we expect, the sidewall angle has very little effect on the beam pattern. Both the narrowing beam and slight gain increase are a result of the beam pattern being truncated by the edge of the parallel plate region.

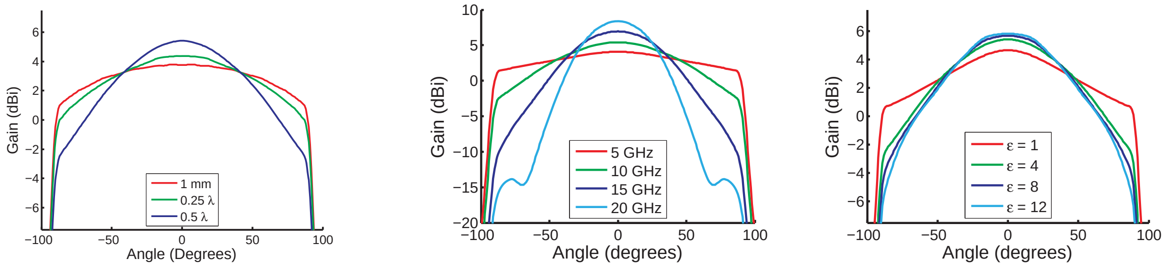

(a) Port Width (b) Frequency (c) Dielectric Constant

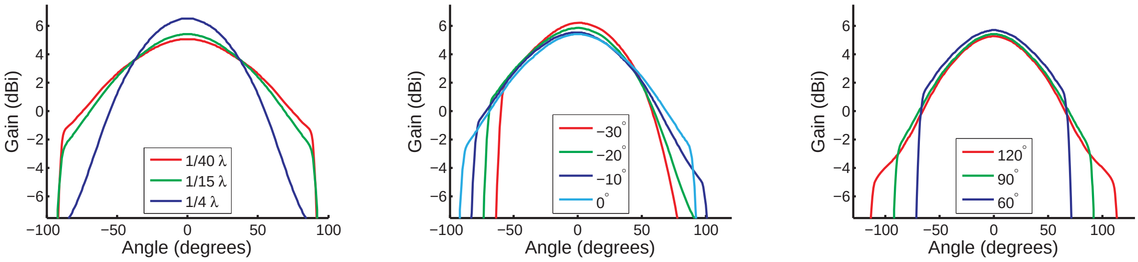

(d) Substrate Height (e) Port Angle (f) Angle of Sidewall

Fig. 7.2: Port beam pattern and port geometry relationship. The two dimensional beam pattern of a single microstrip port is shown here. Each graph varies a single parameter of a reference port constructed using a substrate height of 1 mm, half wavelength width at 10 GHz, 0° port angle and 90° sidewall angle. Subfigures (a) and (b) show that the beam pattern is consistent with that of a two dimensional antenna element. Subfigures (c) and (d) demonstrate that the choice of dielectric constant and substrate height has a noticeable effect on the effective port width. Subfigures (e) and (f) clearly show the truncation of the beam pattern by the sidewall of the infinite parallel plate region, however, this has very little effect on the remaining beam pattern.

7.1.2 Higher Order Port Modes

The results describing the port performance have only considered the primary port mode, because the accepted practice is to limit the port width to a maximum of $\lambda_g/2$. Section 4.3.3 explained that this restriction on port width is to prevent ports from supporting higher order modes and any performance degradation it may cause. However, the severity and nature of this degradation have not been defined. Figure 7.3(a) shows the attenuation of the microstrip port as a function of port width, for the first three microstrip modes. The figure shows that the first mode is supported for all port widths, and therefore the propagation loss remains small, while the second and third modes begin to propagate a little below $\lambda_g/2$ and λ_g respectively. The small reduction in port width that supports the second and third order modes is caused by the increase in effective width of the microstrip line, caused by fringing either side of the port.

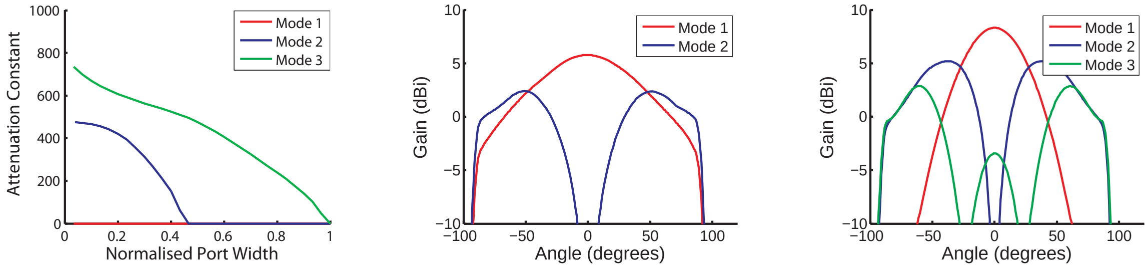

(a) Propagation loss. (b) Port width of $\lambda_g/2$ (c) Port width of λ_g

Fig. 7.3: Higher order port modes. The number of modes supported by a microstrip line is approximately equal to the width of the line divided by $\lambda_g/2$. This has lead to the assumption that ports should be kept less than $\lambda_g/2$ to avoid the effects of higher order modes. These figures show the cut-off frequencies and two dimensional beam patterns of the first three modes of a microstrip line. Subfigure (a) presents the propagation loss of the first three modes while Subfigures (b) and (c) show the beam patterns of the higher order modes for a port width of $\lambda_g/2$ and λ_g. The results demonstrate that second order modes are not strongly excited if the incident angle from boresight remains small. However, the third order mode will significantly degrade the performance of the lens if it is allowed to propagate. The practical implications of this result is that broader bandwidths may be achieved using ports approaching λ_g in width at the highest frequency of operation.

The fields of the first, second and third order microstrip modes differ significantly. The first order mode can be treated as a single uniform excitation across the port. The beam pattern of the first order mode resembles a sinc function with its maximum gain in the direction of the port. The second order mode drives each side of the port 180 degrees out of phase and can be treated as two separate excitations. In the direction of the port, these to waves cancel, causing a null directly in front of the port and two maxima either side. The third order mode can be treated as three separate excitations, the central being 180 degrees out of phase with the outer two. The resultant beam pattern contains three peaks and two nulls. Figure 7.3(b) shows the first and second microstrip mode for a port width of $\lambda_g/2$ and the beam pattern of the first, second, and third microstrip mode for a port of width λ_g, in Figure 7.3(c).

The standard configuration of the microstrip Rotman lens excites the ports using the first order mode. Provided no discontinuities exist in the port, coupling between modes is minimal and the driven port does not suffer any ill effects caused by higher order modes.

However, Figure 7.3 shows that when the port is receiving energy from the body of the lens, the incoming wave may not be uniform in both phase and magnitude across the port interface and strongly excite the second or third order mode. This is particularly relevant when the incoming wave is incident at large angles from boresight. This energy will be reflected back into the lens body or coupled to the first order mode within the matching network.

Ports that are not required to have large angular fields of view, will not be strongly affected by second order modes when port widths are allowed to increase beyond $\lambda_g/2$. Under these conditions the maximum port width can approach λ_g, provided the third order mode is not excited.

7.1.3 Port Phase Centre

The port phase centre is the apparent origin of the circular wavefront when viewed in the far field. The phase centre of each port should be located at the port position determined by the Rotman equations. The accepted approach is to assume that the phase centre of the microstrip port is located in the middle of the port, on the line of intersection between port and body of the lens. The validity of this assumption should be checked as incorrect port positioning causes defocusing of the lens.

Aberrations caused by incorrect positioning of the port's phase centre will be referred to as *port positioning error*. In reality, port positioning error can not be completely removed, instead the location of the phase centre is defined to minimise the phase errors for the port's field-of-view. The port is then placed so that the phase centre of the port, rather than the midpoint of the port junction, is located at the positions defined by the Rotman equations.

The phase centre is found by comparing the phase and magnitude of the E-field at a constant radius from the centre of the port junction. The phase centre is the position that minimises the RMS difference between a wave originating at that position and that excited by the port. The wavefront of the microstrip port is not circular and therefore the RMS phase error will not be reduced to zero. The remaining error is referred to as *port wavefront error*. The magnitude of the port positioning error, and port wavefront error, of any given port implementation is dependent on the geometry of the port and matching structures connected to it.

The model described in Section 4.3.1 has been used to predict the relationship between the microstrip phase centre behaviour and port width, frequency, and port angle. The results of this analysis are shown in Figure 7.4. The subfigures of Figure 7.4 show the position of the phase centre relative to the origin of the port boundary, and the phase errors introduced by the phase variation as a function of angle for both corrected and uncorrected port position error. These figures show that the phase centre is a significant distance from centre of the port junction. Figure 7.4(a) shows that the ports phase centre moves further from the port junction as port width increases. More importantly Figure 7.4(b) demonstrates that the phase centre does not change significantly as the frequency is varied. This suggests that broadband lens designs will not suffer additional errors due to a moving phase centre across the frequency band of operation. The angle of the port has little affect on the distance of the phase centre from the origin of the port, however Figure 7.4(c) shows that the phase centre is offset from boresight as the port angle is increased.

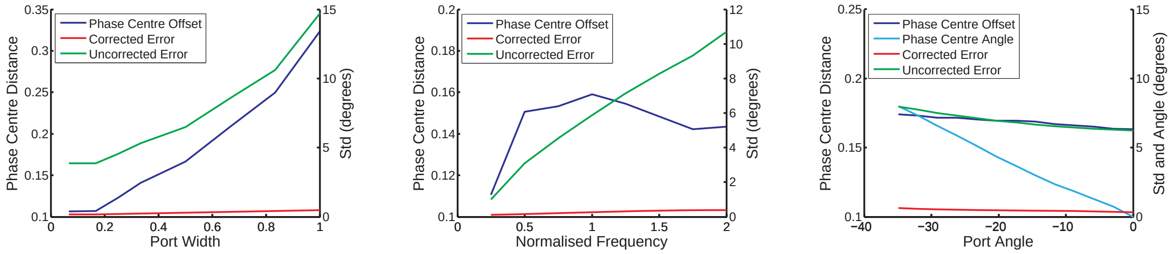

(a) Port Width (b) Frequency (c) Port Angle

Fig. 7.4: Phase centre position. The ideal port junction has a well defined phase centre located at the position defined by the Rotman equations. The microstrip port junction does not have a perfect phase centre and therefore the position of the port must be optimised to minimise these additional phase errors. These figures show the phase centre distance, normalised to the guided wavelength, from the port to lens body intersection. Subfigure (a) plots the phase centre distance to the port width, normalised by the guided wavelength. Subfigure (b) plots the phase centre distance of a $\lambda_g/2$ wide port, at the centre frequency, to normalised frequency. Subfigure (c) plots the variation in phase centre distance and angle as port angle is varied.

The magnitude of these errors is demonstrated by comparing the total RMS phase errors, caused by an imperfect port phase centre, to the geometrical optics RMS phase errors. Figure 7.4 shows that using a uniform port width, a narrow-band lens design using $\alpha = 30°$ and $f = 1$ will need to feed an aperture 1700 wavelengths wide before the geometric error becomes larger than the port positioning error and 120 wavelengths wide before the geometric error becomes larger than the port wavefront error. The significance of incorrect port positioning, due to failing to account for phase centre offset and port wavefront error, should not be underestimated. Section 7.5.2 describes how the ports phase centre offset is included into the design flow of the broadband Rotman lens.

7.1.4 Port Coupling

Coupling between adjacent antenna ports, or beam ports, degrades the performance of the lens by returning energy back into the driven ports or by disturbing the planar wavefront within the body of the lens. Coupling effects are particulary important when considering broadband lens designs. This is because coupling between adjacent ports is increased by the reduced effective port spacing, and port width, at the lower end of the operating bandwidth.

The port model, shown in Figure 7.1(a), has been extended to examine the port properties in the presence of neighbouring ports. The electromagnetic model shown in Figure 7.1(b) has been used to predict the relationship between port coupling, port spacing, and frequency. This work highlights the strong coupling between adjacent ports for narrow port spacing and low frequency. Figure 7.5(a) varies the port spacing between $0.1\lambda_g$ and λ_g, where λ_g is the guided wavelength, while Figure 7.5(b) examines the performance of a $\lambda_{g0}/2$ spaced ports as a function of frequency, where λ_{g0} is the guided wavelength at the centre frequency. As port spacing is reduced below $\lambda_g/2$, the beam port isolation between adjacent ports is degraded. More importantly the insertion loss due to coupling between beam ports becomes significant. Figure 7.5(a) shows that port coupling increases to -3.3 dB as the effective port spacing approaches a quarter wavelength, resulting in 2.7 dB of insertion loss due to port coupling alone. Examination of Figure 7.5(b) shows that if the maximum coupling loss is kept less than 3 dB, and maximum port spacing is $\lambda_g/2$, a microstrip implementation of a Rotman lens is limited to a bandwidth of approximately 1:1.46. To increase the low frequency performance, multiple adjacent ports must be excited simultaneously.

The increased port coupling at lower frequencies causes not only reduced two dimensional aperture gain, but also increased insertion loss. The increased insertion loss prevents energy from propagating through the lens by redirecting it to neighbouring ports, while the reduced aperture gain increases energy lost to the sidewalls of the lens. These effects combine to strongly limit the low frequency performance of the Rotman lens.

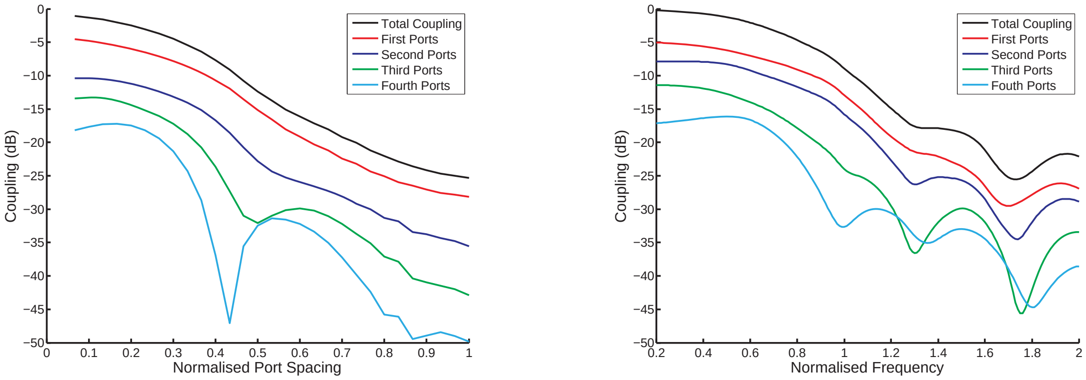

(a) Width and port coupling

(b) Frequency and port coupling

Fig. 7.5: Port coupling. Coupling between adjacent ports of the antenna or focal arc increases the insertion loss and phase errors, and reduces beam port isolation. The relationship between port spacing and coupling is shown in Subfigure (a). The port width is kept 5 % smaller than the port spacing. The relationship between frequency and coupling is shown in Subfigure (b). These figures show that narrow, closely spaced ports, or low operating frequencies increases coupling to a level where most of the energy is coupled to neighbouring ports rather than transmitted through the lens. Therefore, to achieve acceptable performance over broad frequency ranges, widely spaced ports are required.

7.1.5 Port Impedance

The impedance of the port junction has been examined with the intention of simplifying the port impedance matching requirements. The relationship between port impedance and a number of port parameters is shown in Figure 7.6. The fundamental design parameter is port width because it is also the width of the microstrip or stripline at the port junction. The results shown in Figure 7.6 facilitate port geometry and substrate choices that minimise the challenges of matching the port to an undefined length of transmission line.

Figure 7.6(a) shows the relationship between the port and microstrip impedance as a function of port width. As the width increases beyond $\lambda_g/2$, the impedance of the port and the characteristic impedance of the microstrip line become similar. Increasing port width beyond $\lambda_g/2$ allows the port to support the second order mode. As explained in Section 7.1.2, this causes a significant increase in reflections within the body of the lens if the port is excited by waves far away from boresight. This consequently reduces the efficiency of the lens. Below $\lambda_g/2$, the magnitude of the imaginary component of the port impedance grows, as does the microstrip characteristic impedance. The real component of the port impedance continues to rise, but at a significantly slower rate than the microstrip characteristic impedance. This divergence of impedance makes port matching for port widths below $\lambda_g/2$ increasingly challenging. Narrow port widths also require a matching network to cancel the large imaginary component of the port junction impedance.

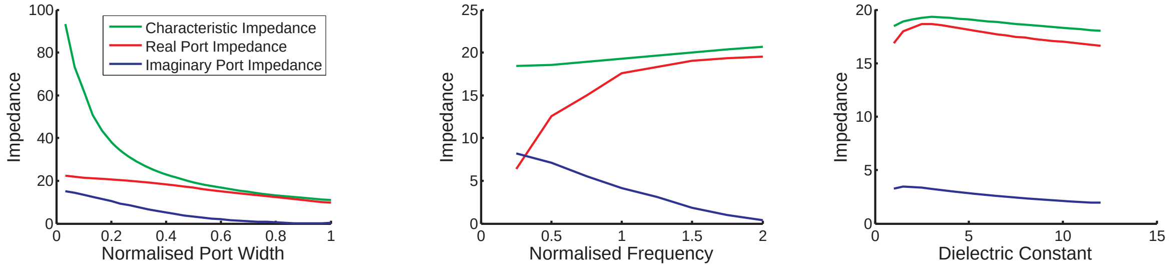

(a) Port Width (b) Frequency (c) Dielectric Constant

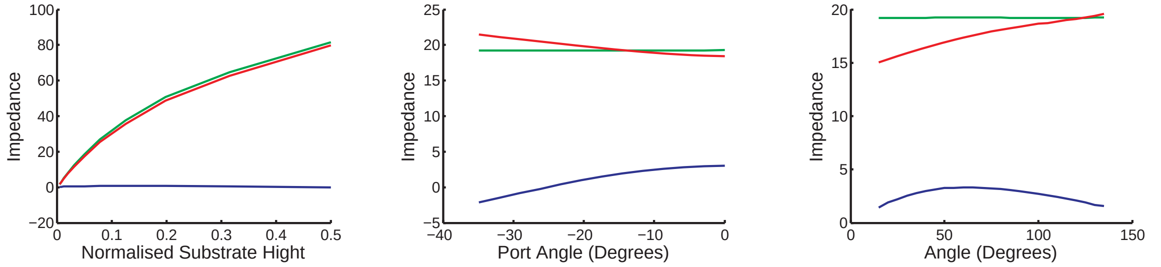

(d) Substrate height (e) Port Angle (f) Angle of Sidewall

Fig. 7.6: Port impedance relationship. The impedance of the port lens interface is controlled by the geometry of the port and the choice of substrate. These figures show typical relationship between port impedance and width, frequency, dielectric constant, substrate height, port angle and sidewall angle. Choosing geometries that keep the imaginary port impedance low, and the real port impedance close to that of the microstrip line, simplify the matching networks required. The results show that port matching will become difficult for narrower ports and higher frequencies while increased substrate height will alleviate this problem. Port and sidewall angle and dielectric constant will have minimal effect on the matching problem.

The effect of frequency and dielectric constant are dominated by their relationship to effective port width. At lower frequencies the effective port width is narrower, reducing the resistance and increasing the inductive reactance of the port compared to the microstrip characteristic impedance. The microstrip characteristic impedance remains relatively constant, only dropping slightly as the frequency is reduced. Increasing the normalised frequency beyond 1 increases the effective port width past $\lambda_g/2$, supporting second order modes and reducing coupling to the outer antenna ports.

Increasing the dielectric constant reduces the wavelength within the parallel plate region, increasing the effective port width. To keep the effective port width constant, the port width is scaled by $1/\sqrt{\epsilon}$. Figure 7.6(c) shows that dielectric constant produces only minor changes in the port and microstrip impedance.

Substrate height varies the effective port width only through the fringing fields either side of the microstrip feed line. Figure 7.6(d) demonstrates that increasing the substrate height increases both the real port impedance and microstrip line characteristic impedance while the imaginary port impedance remains small. This suggests that using thick substrates will simplify port matching and facilitate high frequency implementation.

It is common practice to vary the port angle to better direct energy onto the lens antenna ports. The effectiveness of this approach has been explored by varying the sidewalls of the port between 0° and 30° about the origin of the port. Figures 7.6(e) and 7.6(f) show that both port angle and port sidewall incidence angle have little effect on the impedance of the microstrip port. This suggests that the port impedance is dominated by the effective port width perpendicular to the axis of the port. The shape of the sidewalls, or the presence of well matched ports adjacent the port, has little effect on the port's impedance characteristic.

7.2 Rotman Lens Port Implementation

The previous section has highlighted the limitations of monolithic port performance. This knowledge must be combined with our understanding of the Rotman lens geometry to achieve a practical and effective lens design.

7.2.1 Beam Port Width and Choice of g

To realise an effective Rotman lens design, each port must be implemented using an efficient electromagnetic structure that maximises the energy coupled between the antenna ports and beam ports. The design effort is reduced significantly if similar dimensions are used for all ports around the periphery of the lens. This results in similar matching networks, frequency response and phase delay for all ports. Uniform port width is not achieved by leaving large gaps between ports as these surfaces reflect energy back into the body of the lens, adversely effecting lens performance. The solution is to choose port spacings that keep port width constant.

This simplest lens implementation uses equally spaced beams without a stringent requirement on crossover point. Such a lens is easily implemented by defining $g = 1$ resulting in a constant radius focal arc and constant port width and spacing. A lens design requiring orthogonal beams or beam crossing at the -3 dB point must increase the angular beam port spacing as the beam angle increases. To keep port width constant, the normalised radial distance, h, of the port must be reduced. The radial position for orthogonal, -3 dB, and uniformly spaced beams is shown in Figure 7.7 for port widths of $\lambda_g/2$ and λ_g. At each of the focal points $f = h$, this then defines the value of f yielding a maximum beam port width of $\lambda_g/2$ or λ_g.

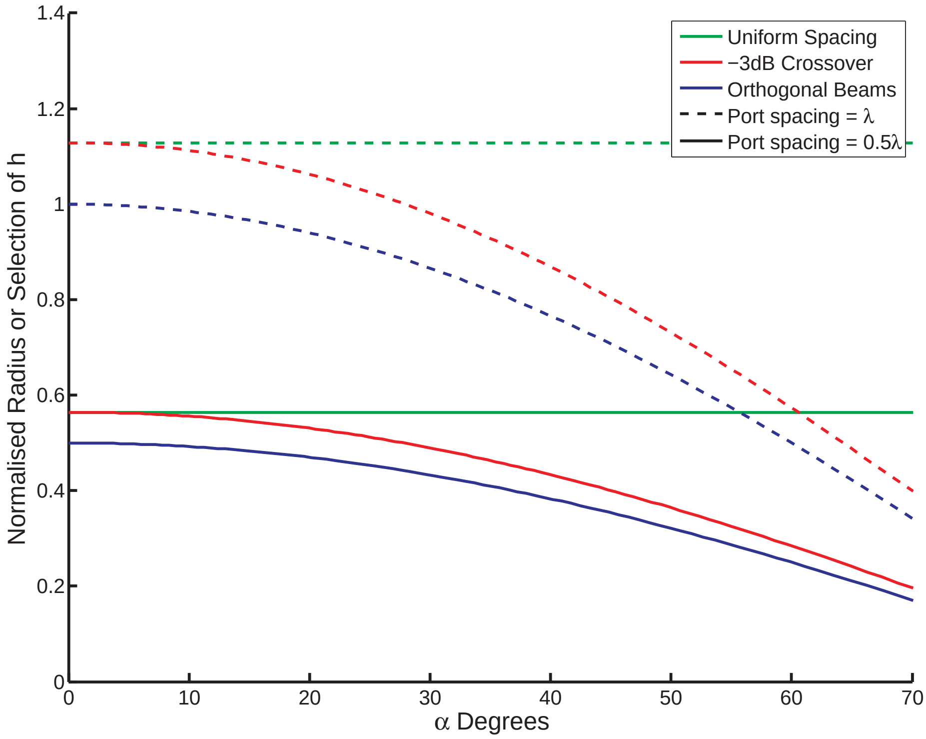

Fig. 7.7: Radial distance of beam port. The position of each beam port should be chosen to achieve specific beam direction or cross over point. Port matching is simplified if port width is kept constant. This figure demonstrates how the radial position of the beam port varies to maintain uniform port width across the focal arc, while achieving uniform beam spacing, -3 dB cross over, and orthogonal beams. Increasing beam width, as α increases, reduces the distance of the beam port from the origin h. The value of h at the maximum beam angle and $\alpha = 0$ is used to define f and g.

The relationship between beamwidth and α can be calculated by noticing that

$$\Delta\phi = \frac{BW_0}{\sin(\phi)},$$

as explained in Section 2.2.2, where $\Delta\phi$ is the angular width of the beam port and $\phi = \pi/2$ for a broadside beam. Using the design variables and the focal arc geometry defined in Figure 4.3,

$$\Delta\phi = \frac{BW_0}{\cos(\theta)},$$

the size of the port, d, is given by

$$\begin{aligned} d &\approx H\Delta\phi, \\ &\approx H\frac{BW_0}{\cos(\theta)}. \end{aligned}$$

If the port width, d, is kept constant for all α,

$$H = G\cos(\theta),$$

and at the two outer focal points,

$$F = G\cos(\alpha).$$

Therefore g is given by,

$$\begin{aligned} g &= \frac{G}{F}, \\ &= \frac{1}{\cos(\alpha)}. \end{aligned} \tag{7.1}$$

Therefore, uniform beam port width across the focal arc for both orthogonal and -3 dB beams is achieved by setting $g = 1/\cos(\alpha)$, as suggested by Smith (1982).

7.2.2 Sub-Port Design

Section 7.1.4 explains that both bandwidth and efficiency is improved by increasing the effective port width beyond $\lambda_g/2$. However, if higher order modes are to be avoided, Section 4.3.3 suggests that each port should be broken into multiple sub-ports and fed using individual sources or a power splitting network. Narrow-band lenses use this technique to improve efficiency and reduce sidelobes by implementing an excitation taper across the lens contour.

Higher order modes remain a problem in sub-port Rotman lens implementations. In a dual sub-port design, higher order modes are present in the form of odd and even mode excitation of two sub-ports. The odd mode closely resembles the second order mode in a single port design except it is now present at all frequencies. A sub-port implementation does facilitate the removal of the odd mode. This is done by absorbing it using a Wilkinson divider, preventing the energy from being reflected back into the lens or coupled to the even mode.

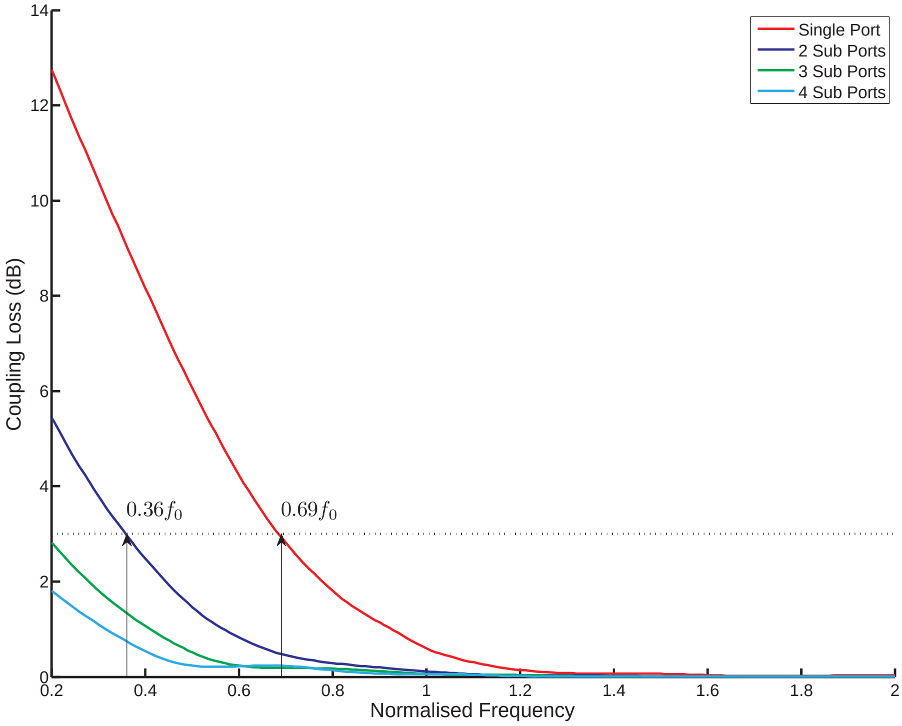

Fig. 7.8: Sub-port coupling loss performance. Lenses that replace the individual beam ports with small arrays of sub-ports, of equal width, decrease the coupling between adjacent beam ports. These lenses exhibit lower coupling loss and the stronger excitation taper reduces sidelobe levels. Broadband lenses low frequency performance is improved due to reduced impedance variation synonymous with lower port coupling.

The improvement in gain, caused by driving multiple perfectly matched sub-ports, is demonstrated in Figure 7.8. As the number of driven sub-ports is increased, the effective port width is increased and coupling loss is reduced. Figure 7.8 demonstrates that a lens design using two or three uniformly excited sub-ports reduces the frequency of the 3 dB coupling loss point from 0.69 f_0 for a single port to 0.36 f_0, and < 0.2 f_0 respectively.

7.2.3 Antenna Port Design

The requirements of antenna ports are different to beam ports. While it is beneficial to increase the width of the beam ports to produce an excitation taper across the lens contour, increasing the width of antenna ports will reduce the coupling to the outer beam ports and reduce the efficiency of those beams.

The position of the antenna ports and their spacing is dependent on the positions of each element of the array and the value of the variable β. For lenses with $\beta = \alpha$, the antenna ports have a similar spacing to the elements of the array. Therefore the rules governing the size of the antenna array and the spacing of its elements will tend to be applied to the lens contour and the positions of the antenna ports.

Array elements are spaced as widely as possible, while avoiding grating lobes appearing when the outermost beams are excited. A narrow field-of-view allows increased array element spacing and width, and therefore accommodates increased antenna port spacing and width. Grating lobes limit the distance between array elements to d, calculated using the formula:

$$d < \frac{\lambda}{1 + |\cos \beta|},$$

where β is the desired field-of-view of the array and lens. Choosing d to be as large as possible without introducing grating lobes maximises the gain of the array. Therefore, antenna port spacing will tend to be $\geq \lambda_g/2$ at the highest frequency of operation, for $\alpha = \beta$.

The variable α is free to optimise the antenna port width without affecting the field-of-view, or beam port spacing. Reducing α will increase the width and two dimensional beamwidth of each antenna port, it will also reduce the angular width of the focal arc. Therefore, the efficiency of the outer beam ports should not be severely affected by the choice of α.

7.2.4 Sidewall and Dummy Port Design

Historically reflections from the sidewalls are the biggest limiting factor affecting the beamforming performance. The Rotman design equations do not specify the shape of the sidewall that joins the lens focal ports to the lens array ports, therefore the sidewalls can be freely designed to minimise the reflected wavefront within the lens. Two practical approaches have been described in Section 4.3.4. RAM placed along the sidewalls of the lens is most commonly used in waveguide based designs while microstrip and stripline implementations generally replace the air within the body of the lenes with an alternate dielectric making radiation absorbing material impractical. In these circumstances dummy ports terminated in matched loads are added along the sidewalls of the lens.

Sidewall Geometry

The shape of the lens sidewall dictates how efficiently energy encountering the wall is absorbed. A perfect sidewall absorbs all energy from all incidence angles and can be implemented as a straight edge connecting the ends of the focal arc and lens contour. If the sidewall is imperfect the absorbtion of energy is only effective over a limited range of incidence angles, the remaining energy is reflected back into the body of the lens.

Like the beam and antenna ports, the field-of-view over which lens sidewall is effective is limited. For maximum performance, the beam ports and antenna ports must be kept within this field-of-view as much as possible. The effectiveness of the sidewall will also be improved if wavefront must undergo multiple reflections off the sidewall before encountering another beam or antenna port. This is because each encounter with the sidewall absorbs more energy.

A typical orientation for well designed sidewalls is shown in Figure 7.9. This involves invoking two sections of sidewall, one absorbing radiation from the antenna ports and the other absorbing radiation from the beam ports. This keeps most of the incident energy within a narrow field-of-view. The energy from the ports outside the effective field-of-view is reflected onto another section of sidewall.

7.3 Impedance Matching

Directly connecting a transmission line of arbitrary length to the body of the lens generally results in large reflection loss. This is avoided by introducing an impedance matching network to present a more optimal load to the port. The long tapered microstrip line and multisection quarter wavelength impedance transformers, introduced in Section 4.3.3, have been demonstrated effectively in the literature.

The tapered line relies on a poorly defined but gradual impedance taper over multiple wavelengths and a wide port ensuring the imaginary component of the port impedance is

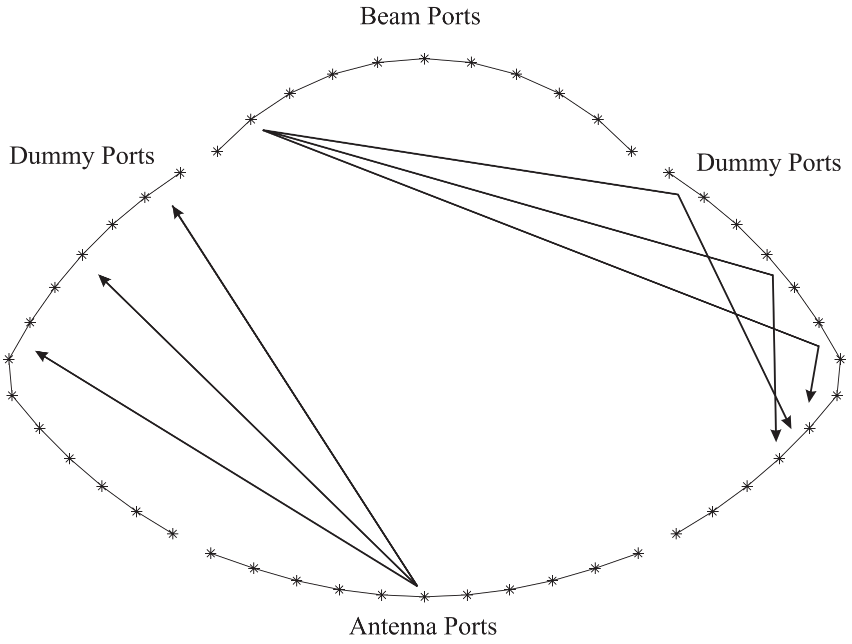

Fig. 7.9: Sidewall design. The lens sidewall absorbs any part of the wavefront not collected by the antenna contour or focal arc. This prevents the energy being reflected back into the lens body causing additional sidelobes or beam port coupling. The sidewall will absorb energy from some angles better than others. A sidewall should be orientated so that any incident wave must undergo multiple reflections before re-entering the body of the lens.

small. A typical example is shown in Figure 7.10(a). Figure 7.10(c) shows an exponential impedance taper which implements a precise impedance taper over $\lambda_g/2$ at the lowest frequency of operation. This results in a good match at all frequencies above the design frequency. Like the linear taper, the exponential taper matches to a purely real impedance, however the exponential impedance taper can be made much more compact and for a given bandwidth. Figure 7.10(c) shows an example of a multisection matching network. These matching networks rely on precise knowledge of the port impedance and accurate layout. Their advantage is that they are able to match to a complex port impedance over a wide bandwidth.

The matching technique suggested by Chan et al. (1994), and described in Section 4.3.3, is appropriate for finding the source impedance of each individually excited beam port. This has been a relatively successful approach but relies on low coupling between all ports and does not consider multiple port excitation. This method assumes that adding the matching network to each port on the lens will result in negligible changes in the impedance of all other ports. To find the optimal beam sub-port or antenna port source impedance a new methodology has been adopted.

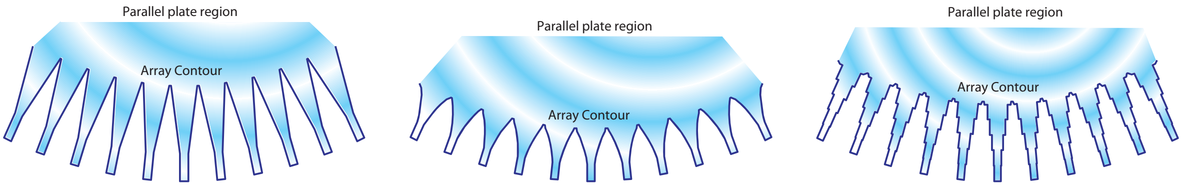

(a) Linear Tapered Port (b) Exponential Tapered Port (c) Impedance Matched Port

Fig. 7.10: Port design. Simple lens designs have used the linear tapered port, Subfigure (a), because of its simplicity. The exponential tapered port and the multi segment impedance matched port shown in Subfigures (b) and (c) require precise knowledge of the impedance at each port. The lenses described in this chapter will use these port geometries because of the precise impedance control they provide, compared to the linear tapered port.

Once the impedance of a port is determined, a matching network must be designed to present a complex conjugate load to the port to achieve a perfect match. When impedance matching multiple coupled ports, the presence of the new load impedance at any single port alters the impedance required to match all other ports. The task is to find a unique broadband match, simultaneously, at all ports.

7.3.1 Sub-Port Impedance Matching

The impedance matching method described in Section 4.3.3 assumes that all ports are being driven independently. The matched condition means that when any port is excited, no power is reflected back from the port. All other ports absorb power based on the coupling between that port and the driven port. If this method is used to match sub-ports, energy coupled between sub-ports will be absorbed by the source driving each sub-port. This method will result in similar coupling losses experienced by single port lens designs.

When separate sources are used to drive each port, as depicted on Figure 7.11, each sub-port should not be treated independently of all others. The sub-ports are properly matched when the energy reflected back to the source from each sub-port is cancelled by the coupled energy from the remaining excited sub-ports. To account for this port matching condition, the method described earlier must be extended.

Using the power-wave formulation of S-parameters, the input impedance of each port is calculated. However, we are no longer interested in the input impedance of a single port, instead we are interested in the apparent input impedance when all sub-ports are being

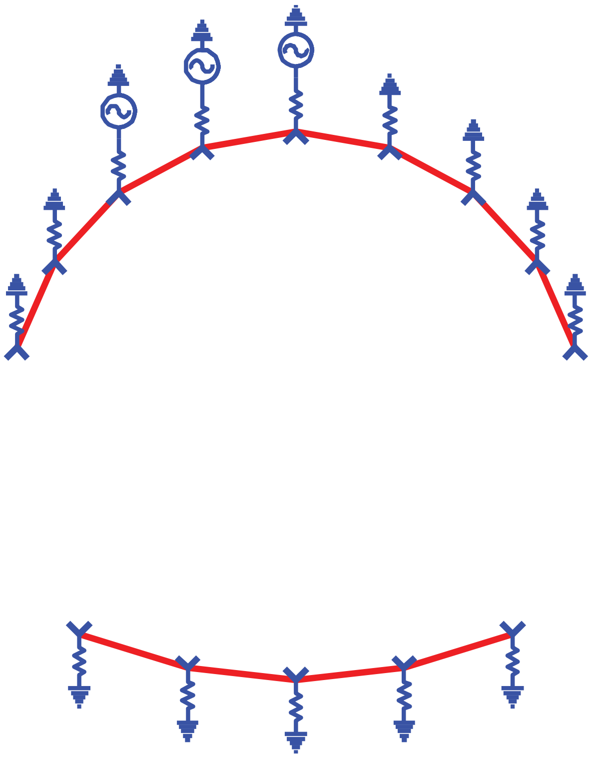

Figure 7.11: Port matching. Sub-ports are excited together with a constant magnitude and phase relative to each other. Each port is matched to the apparent input impedance of the network, while all ports are excited. This input impedance is derived from the combination of the reflected wave and the waves coupled from all other sub-ports.

excited. This is achieved using the following approach. The input impedance of port i is calculated using:

$$\mathbf{Z}_{\mathrm{in},i} \quad = \quad \Re(\mathbf{Z}_{\mathrm{ref},i})\Re(z) + \jmath(\Re(\mathbf{Z}_{\mathrm{ref},i})\Im(z) - \Im(\mathbf{Z}_{\mathrm{ref},i})).$$

Instead of calculating z using $z = \frac{1+\mathbf{S}_{ii}}{1-\mathbf{S}_{ii}}$, the outgoing wave at port i is used, $\mathbf{b}_i$. Thus z is calculated using:

$$z \quad = \quad \frac{1+\mathbf{b}_i}{1-\mathbf{b}_i},$$

where

$$\mathbf{b} = \mathbf{S}\left(\frac{1}{\mathbf{a}_i}\mathbf{a}\right),$$

and $\mathbf{a}$ is the excitation the lens experiences due to the group of sub-ports that comprise port i. The factor $1/\mathbf{a}_i$ renormalises the input excitation by that of port i. For a single port system this method is equivalent to that of Section 4.3.3. For the case of multiple sub-ports, this results in no power being lost to the sub-ports while being excited by the same magnitude and phase defined by $\mathbf{a}$.

By repeating this process for all groups of sub-ports in the same way described in Section 4.3.3, the source impedances converge on the optimal values. The presence of multiple adjacent ports increases the real port impedance above that required of an isolated port for lower frequencies. The ideal source impedance attached to each port of a N sub-port system is shown by Figure 7.12. The figure shows that as ports are combined into multiple sub-ports, the variation of real impedance is reduced and the imaginary component becomes closer to zero. The net effect is that much simpler matching networks are used on each port.

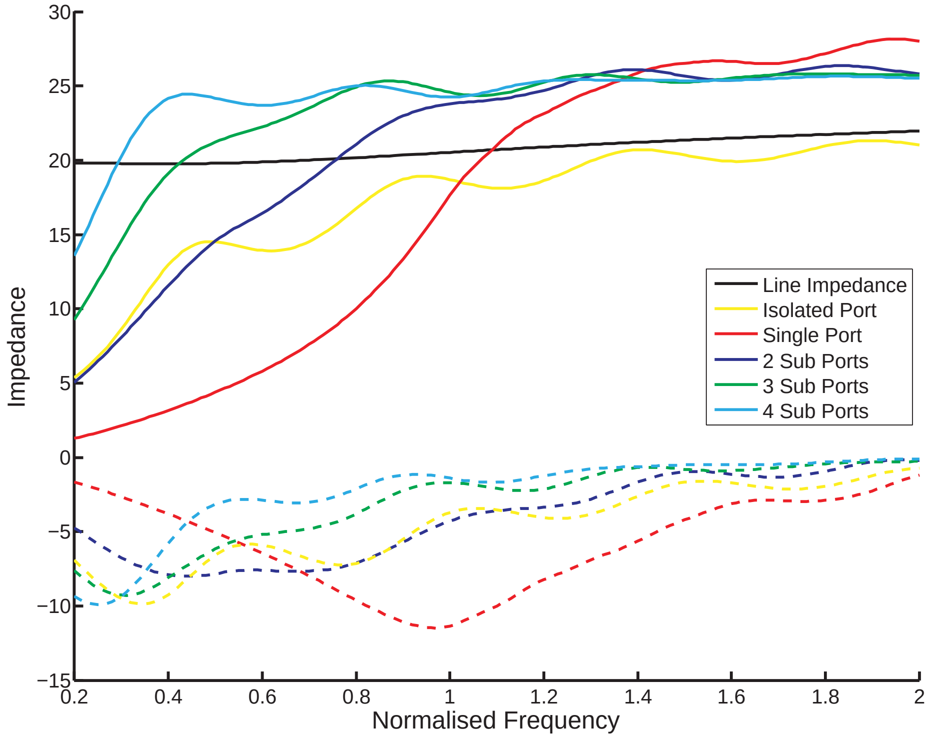

Figure 7.12: Sub-port input impedance. Increasing the number of sub-ports increases the effective port width and reduces the variation of input impedance over frequency. The reduced real impedance variation, shown by the solid lines, and imaginary impedance magnitude, the dashed lines, simplifies the task of matching.

7.3.2 Antenna Port Matching

The impedance matching requirement of the antenna port array is one of the primary performance limitations of the Rotman lens. This is because the antenna array has a varying magnitude and phase gradient depending on which beam is being excited, making it impossible to perfectly match all beams simultaneously.

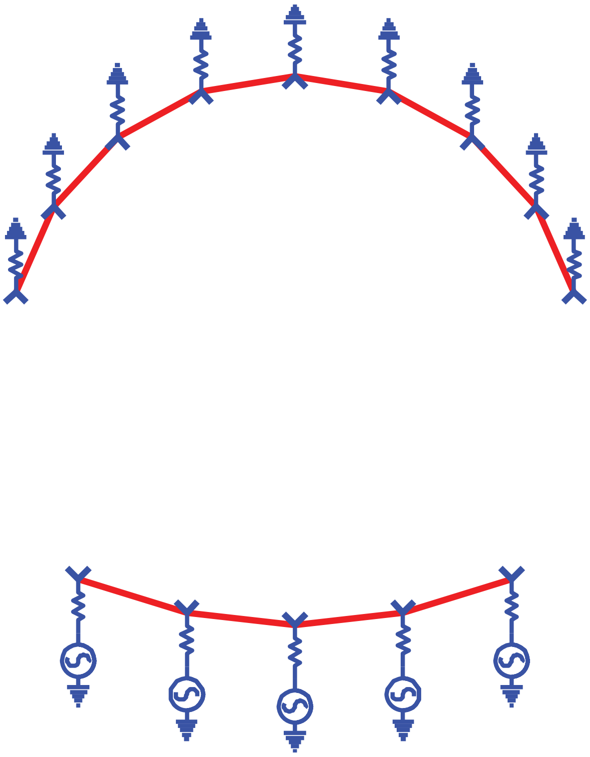

Figure 7.13: Port matching. When the antenna elements are connected directly to the antenna array, the antenna ports are excited by a constant magnitude but a variable phase gradient related to the incident angle of the wave. The reflection coefficient associated with each beam angle is calculated and the mean is used to calculate the desired port impedance.

To demonstrate the importance of antenna port matching three methods have been used to match a twelve port network, similar to that shown in Figure 7.1(b). To demonstrate the effectiveness of these three methods, Figure 7.14 shows the reflection loss, the total energy reflected back to the antenna array from the Rotman lens, and the optimal port impedance for each method. The first method is described in Section 4.3.3 and is shown in Figures 7.14(a) and 7.14(d). This method selects port impedances that minimise the return loss when each port is excited individually. This method will allow a narrow-band lens to achieve 100° field-of-view with 4 dB of reflection loss, however, there is little scope to increase bandwidth.

The second method, described in Section 7.3.1, minimises reflection loss for all ports excited with the same magnitude and phase. Figures 7.14(b) and 7.14(e) show that a narrow-band lens using this method could achieve a field-of-view of 80° with 4 dB reflection loss, while only achieving 30° at half the design frequency. This method results in perfect match of the 0° phase gradient.

The final approach, described here, assumes a uniform magnitude but a variable phase gradient consistent with beams at ±50°, ±25° and 0°. The results shown in Figures 7.14(c) and 7.14(f) demonstrate that a field-of-view of $>100°$ is achievable by a narrow-band lens. This method also achieves a 40° field-of-view at half the design frequency and 20° at one quarter of the design frequency.

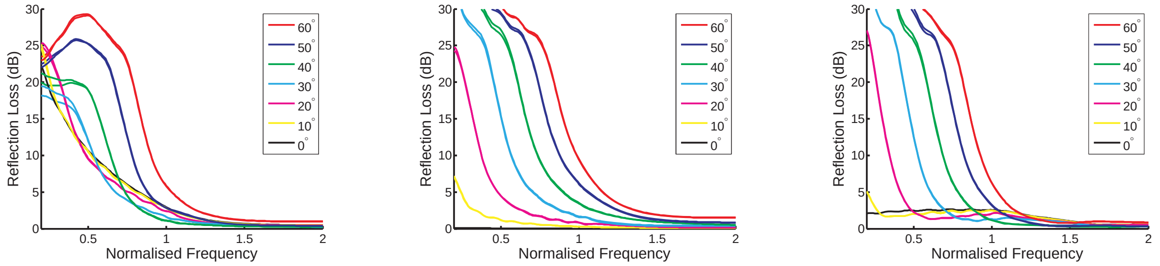

(a) Single port matching (b) Sub-port matching (c) Antenna port matching

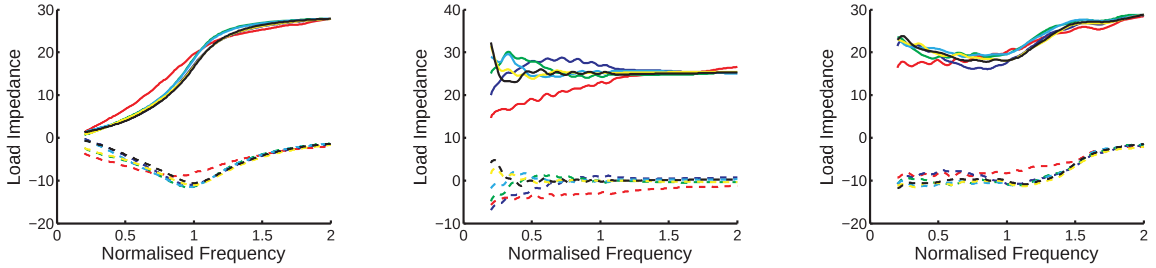

(d) Single port matching (e) Sub-port matching (f) Antenna port matching

Fig. 7.14: Antenna port matching. The three matching techniques described have been used to match a linear array of twelve antenna ports showing reflection loss and real and imaginary impedance (solid and dotted lines). Single port matching performance is shown in Subfigures (a) and (d). These figures demonstrate how the low frequency performance suffers due to reflection loss, and the calculated input impedance varies very quickly with frequency. The sub-port matching techniques broadband performance is very good for a single phase gradient as seen in Subfigures (b) and (e). To achieve both broad bandwidth and significant field-of-view, the antenna port matching system must be used. The antenna port system achieves broadband performance at a range of phase gradients. Subfigures (c) and (f) show both an improvement in reflection loss with both frequency and phase gradient, and less variation in impedance between ports.

The antenna port matching is achieved in the same way as multiple sub-port matching described in Section 7.3.1. The sub-port matching approach assumes constant phase of each sub-port excitation. This is no longer valid for antenna ports as the relative phase varies with the direction of the incoming planar wave or the excited beam port. To achieve optimal match for all antenna ports, the reflected power-wave from port i is calculated for the excitation $\mathbf{a}$, associated with the incoming planar wave that would excite each antenna port. This can be expressed as:

$$\begin{aligned} \mathbf{a}_i &= 1 \\ \mathbf{a}_j &= e^{j\phi_j} \\ \mathbf{a}_k &= 0, \end{aligned}$$

for j is all antenna ports except i, k all other ports and ϕ_j is the angular displacement of port j from the port of interest, i, for a given wave front. The source impedance of each antenna port is calculated based on the mean reflected power-wave from all planar wave fronts. The procedure is repeated until values of $\mathbf{Z}_s$ have converged. In contrast to the method described in Section 7.3.1, the reflected power-waves will not disappear for any combination of realised excitations since this process minimises array return loss, defined in Section 6.3.2, for all realised excitations rather than just one.

This approach is also applicable to sub-ports shared between two beam ports. In this case the reflected power-wave is averaged between the two excitations associated with the two beam ports.

7.3.3 Dummy Port Matching

Dummy port matching is challenging because they are a passive port, making it difficult to choose the excitation $\mathbf{a}$ for optimal performance. The dummy port layout described in Section 7.2.4 can be thought of as four separate port groups, two each side of the beam ports and two each side of the antenna ports. When a single beam port is excited, the energy will propagate across the lens body and impact not only the antenna ports but also the dummy ports on either side. It follows that the these dummy ports and antenna ports will be best matched in a similar way.

The antenna port matching technique has been applied to the dummy ports by treating the dummy ports either side of the antenna ports separately. Each set of dummy ports, plus the two neighbouring antenna ports, are excited with magnitude 1 and the phase is calculated to focus the energy onto each beam port. The mean return power-wave from each dummy port is used to calculate the optimal load impedance, in the same method used to match the antenna ports.

The dummy ports, either side of the focal arc, do not present an obvious choice of excitation. This is because when acting in receive mode, the antenna ports direct energy onto a single beam port. As a result, these dummy ports have only a small effect on the performance of the lens. Due to the erratic wave environment these ports operate in, they may be treated as a group of uniformly excited sub-ports, or a group of individually excited ports. Both choices result in similar lens performance, however the sub-port matching method will yield more convenient port impedances.

7.4 Microstrip Terminations

A novel method of terminating microstrip and stripline transmission lines is now presented. This method provides a matched termination without using plated through holes or vias. This method is ideal for the termination of the dummy ports on the printed lens structures described in this thesis. These terminations exhibit a well defined, and potentially broadband, matched termination for microstrip and stripline applications. The matching structure is easy to design, low-cost, compact and convenient to manufacture, making it useful in high frequency electromagnetic circuits.

These terminations are divided into narrow-band and broadband terminations. The narrow-band termination is constructed using a quarter wavelength section of resistive film. The short length of lossy transmission line acts as an open circuited quarter wavelength transformer. The additional losses in the transmission line move the reflection coefficient away from the periphery of the Smith chart as the length of the line increases, as illustrated in Figure 7.15. As a result, the input impedance is not $0\,\Omega$ as is expected from a quarter wavelength lossless transmission line. Instead, the input impedance has a real value based on the width of the lossy line and the impedance of the resistive film.

The broadband termination has a minimum length of half of a guided wavelength at the lowest frequency of operation. The broadband termination is designed to behave as a long lossy transmission line. By ensuring that losses along the length of the line are greater than 5 dB, a wave propagating to the end of the line and back will experience a loss of 10 dB. Therefore, the reflection coefficient at the input of the lossy transmission line will be less than -10 dB, an acceptable match. The quality of the match is improved further by increasing the loss per unit length along the length of the line. The many reflections caused by the tapering the line, tend to cancel at the input of the line.

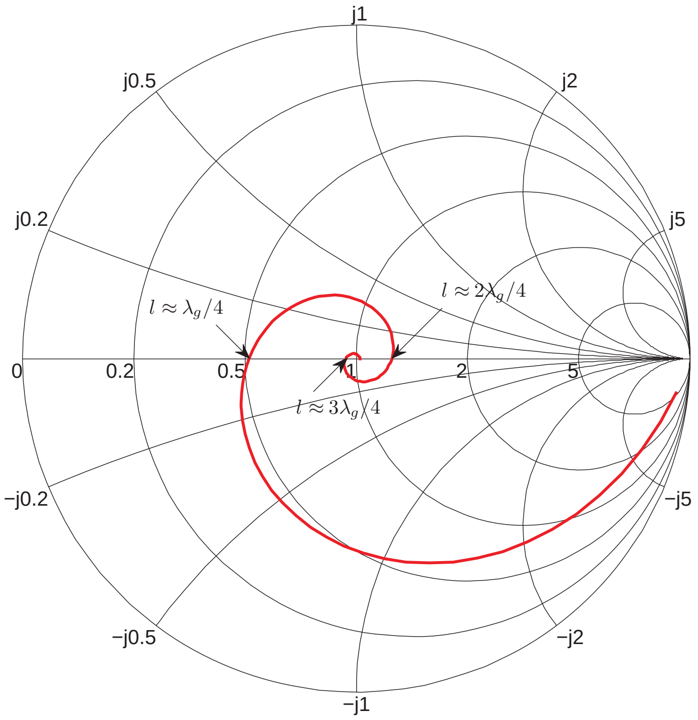

Figure 7.15: Lossy transmission line. Instead of circling the circumference of the Smith chart like the loss less transmission line, the lossy transmission line spirals into the Smith chart. The centre of the spiral is equal to the characteristic impedance of the lossy transmission line. As the length of the line becomes longer, the input impedance varies less with length and therefore frequency.

The quarter wavelength load has been used to terminate the dummy ports of the two narrow-band Rotman lenses presented in Section 7.5.1. To demonstrate the feasibility of such a structure, and to test the accuracy of Ensemble 6.1, the matched load in Figure 7.16(a) was fabricated. The measured results shown in Figure 7.16(b) demonstrate a match better than -13 dB across the entire measured bandwidth and a close agreement with the performance predicted by Ensemble 6.1. The variation between measured and simulated results is a consequence of the test structures finite ground plane and the additional coaxial to microstrip transition.

The size and complexity of the dummy port load depend on the required bandwidth. Figure 7.17 shows three loads and the associated reflection coefficient. The two terminations are constructed using Ohmega-Ply thin film resistors. The first is a quarter wavelength narrow-band load, and the second is a broadband half wavelength load. The final load

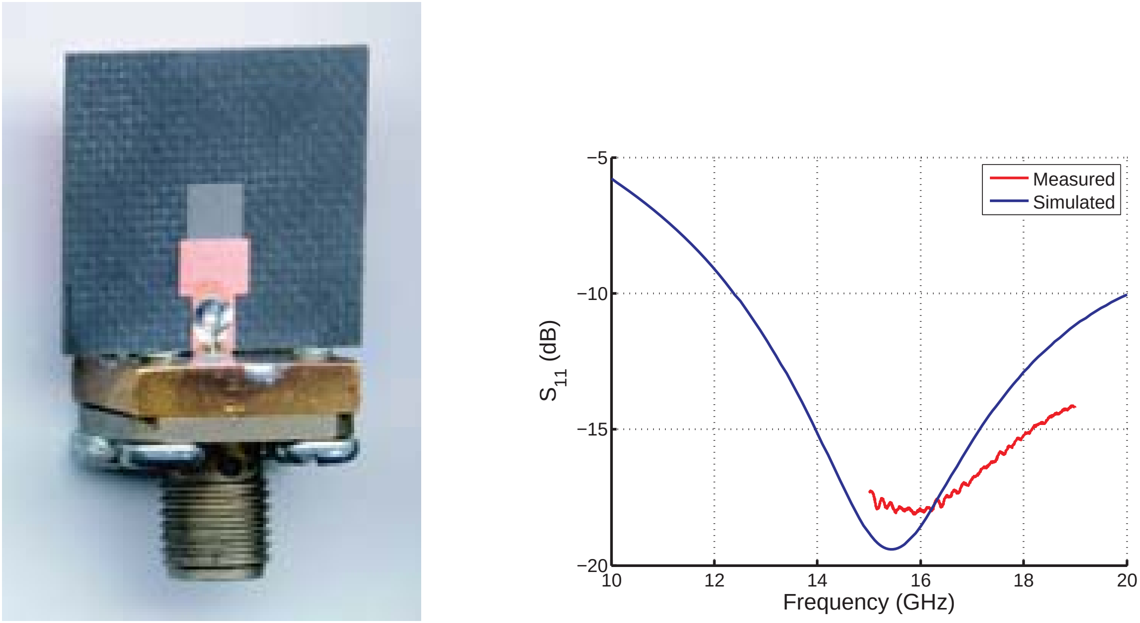

(a) Narrow-band load test structure (b) Measured and simulated results

Fig. 7.16: Termination implementation. This photo depicts our fabricated 50 Ω coax to microstrip transition followed by a quarter wavelength transformer to 25 Ω then terminated with a matched load. The matched load is achieved by our novel lossy transformer with distributed load resistance, constructed using Ohmega-Ply. The performance of this device is shown in Subfigure (b). This graph shows that the results simulated by Ensemble closely resemble the measured results. The performance predicted using transmission line theory do not agree as closely with the measured results. This demonstrates the need for final optimisation using a full-wave software simulation tool.

is a broadband load constructed using Electrodag PR-406 printed resistors. This load is much larger because the Electrodag PR-406 has a 10 Ω/square impedance while the Ohmega-Ply has an impedance of 25 Ω/square. Additional size is also needed to ensure a good match despite the poor manufacturing tolerance of Electrodag PR-406. The Electrodag PR-406 broadband load is used to terminate the dummy ports of the broadband Rotman lens presented in Section 7.5.2.

7.5 Lens Design and Implementation

This section will attempt to bring together all that has been presented. The Rotman lens is a mere mathematical curiosity without an application or system to apply it to. Its purpose is to drive a linear antenna array or similar time delay device. A theoretical

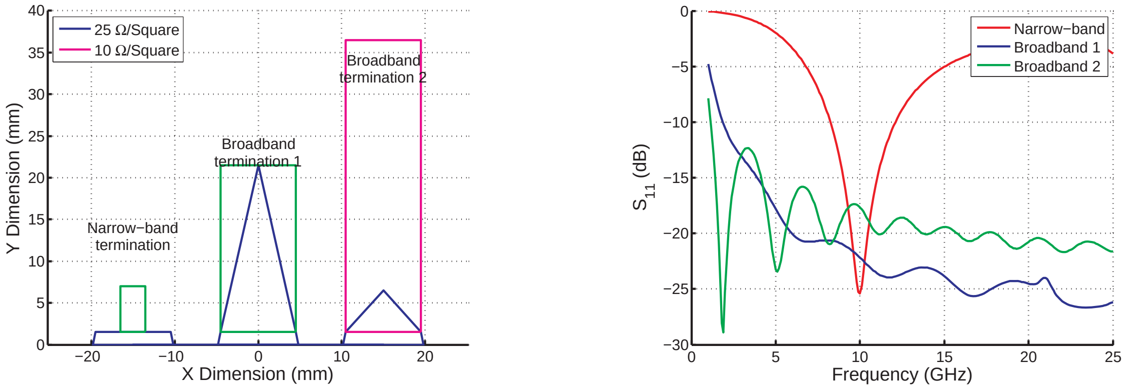

(a) $\alpha = 22.5°$, $f = 0.8333$, $g = 1.0635$

(b) Reflection

Fig. 7.17: Three loads. Three load designs are shown in Subfigure (a) and the performance is shown in Subfigure (b). The first two loads are constructed using Ohmega-Ply, while the last uses Electrodag PR-406. The second and third loads are designed to operate over a broadband. The additional size required for the second load is due to the lower impedance and increased manufacturing variation of the Electrodag PR-406 thick film resistance.

idealised design must be implemented using real imperfect devices, and finally connected to the rest of the system.

7.5.1 Early Lens Designs

The following lenses have been manufactured using RT/Duroid 5880 High Frequency Laminate with a dielectric constant of 2.2 and a thickness of 0.762 mm. Dummy ports have been implemented using a thin Nickel layer with an impedance of 50 Ω/square. This layer is etched to create the 25 Ω matched loads at each dummy port. The materials and frequency of operation of these lens designs have been chosen to demonstrate the potential of such a lens design at 100 GHz by using a substrate thickness of 0.127 mm and reducing the geometry by a factor of 6.

A feature of these lens designs is the integrated patch antenna array resulting in an all-in-one beam-forming network. Each patch antenna element has been offset using zoning, explained in Section 2.4.1, to reduce mutual coupling and increase the gain of the array.

An integrated antenna array prevents the S-parameters of the lens from being measured directly. Instead, the performance of these lens designs must be inferred by the array gain patterns, reflection coefficients, and coupling between beam ports. The narrow bandwidth of the patch antenna, shown in Figure 7.18, also limits the bandwidth available to evaluate the lens performance. The broadband lens of Section 7.5.2 has been implemented without an integrated antenna array so that the lens may be characterised without these limitations.

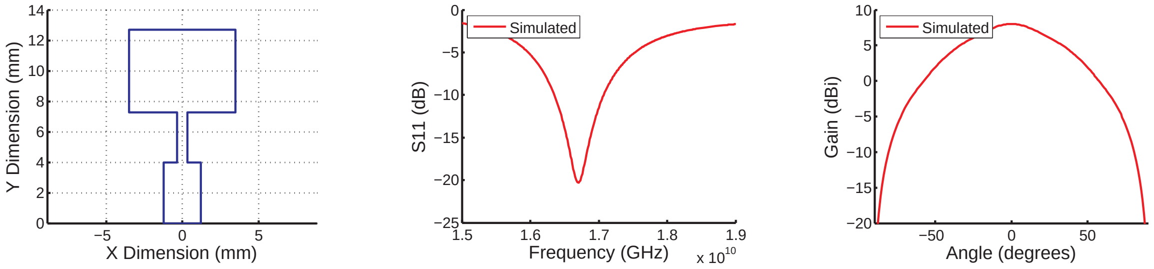

(a) Microstrip Patch (b) Reflection Coefficient (c) Beam Pattern

Fig. 7.18: Microstrip patch performance. The layout, reflection coefficient, and beam pattern of the microstrip patch antenna used in the early lens implementations. By comparing the reflection coefficient of the antenna element and the two lenses, it is apparent that it is the antenna reflection coefficient that limits these systems.

Basic Rotman Lens

This design represents a simple Rotman lens implementation at 17 GHz. Quarter wavelength impedance transformers are used to match the 50 Ω microstrip line to the body of the Rotman lens. The dummy ports are connected to 25 Ω loads by a quarter wavelength transformer.

This lens has been designed in three steps. First, the body of the lens is generated and the beam, antenna and dummy ports are added, shown in Figures 7.19(a) to 7.19(b). The beam ports and antenna ports are constructed using half wavelength tapers extending the body of the lens radially from the central port on the opposite side of the lens. The dummy ports are uniform width lines connected at right angles to the lens body. The length of the dummy ports are staggered by one half wavelength to enable enough room for each matched load and quarter wavelength transformer to be implemented without overlapping its neighbors.

The impedance characteristics of each port of the structure shown in Figure 7.19(b), is calculated using Ansoft Ensemble. The iterative matching procedure described in Section 4.3.3 is used to calculate the desired matching impedance of each port. The quarter wavelength matching sections and matched loads are added as shown in Figure 7.19(c).

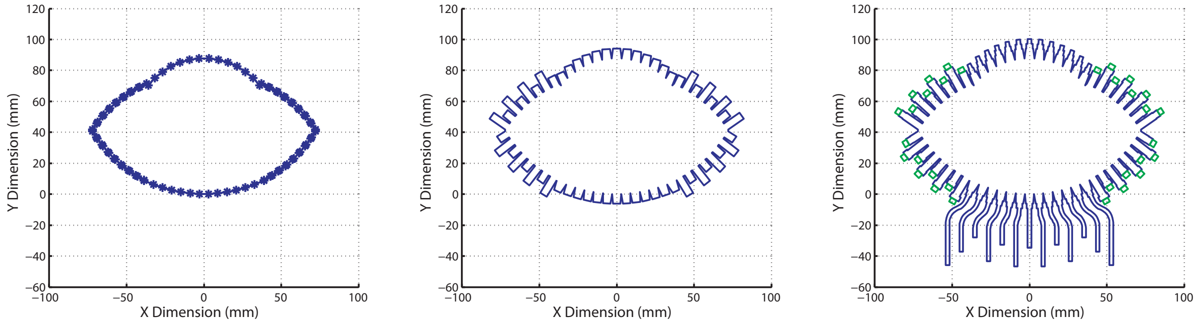

(a) Stage 1 (b) Stage 2 (c) Stage 3

Fig. 7.19: Lens build stages. The three lens layout stages are shown. Stage 1 defines the position of each beam port, stage 2 specifies the outer contour of the lens and is simulated to find the required port impedances. Stage 3 includes all impedance matching networks, dummy port loads and transmission lines.

Furthermore, one wavelength radius meander lines are added to the antenna ports and the structure is simulated again. This is carried out because the phase delay of circular transmission lines is difficult to characterise.

After simulating the lens again, the expected performance of the lens is evaluated. This simulation shows that all ports are well matched at 17 GHz and the phase error across the focal arc is less than 5°. As expected the single beam port design suffers significant insertion loss due to energy absorbed primarily by the sidewalls of the lens. Figure 7.20(a) shows that sidewall loss contributes most of the insertion loss, 3.6 dB to 5.2 dB, while reflection loss and coupling loss contribute 0.15 dB. The expected excitation taper across the antenna array is shown in Figure 7.20(b). Excluding the outermost ports, excitation of the antenna port vary by only 1 dB.

The relative phase delay of each antenna feed line has been calculated while driving each beam port. The lengths of the antenna feed lines are tuned to minimise phase errors of all beams. The final Rotman lens layout is shown in Figure 7.21.

The lens has been characterised using a two port Wiltron 37369A Vector Network Analyser (VNA) from 16.25 GHz to 17.25 GHz. The two port scattering parameters have been measured between each pair of ports while all other ports are terminated using a 50 Ω load. These two port scattering parameters have been combined to form the 13 port scattering matrix. These have been summarised in Figure 7.22. The beam pattern has also been measured and is shown in Figure 7.23.

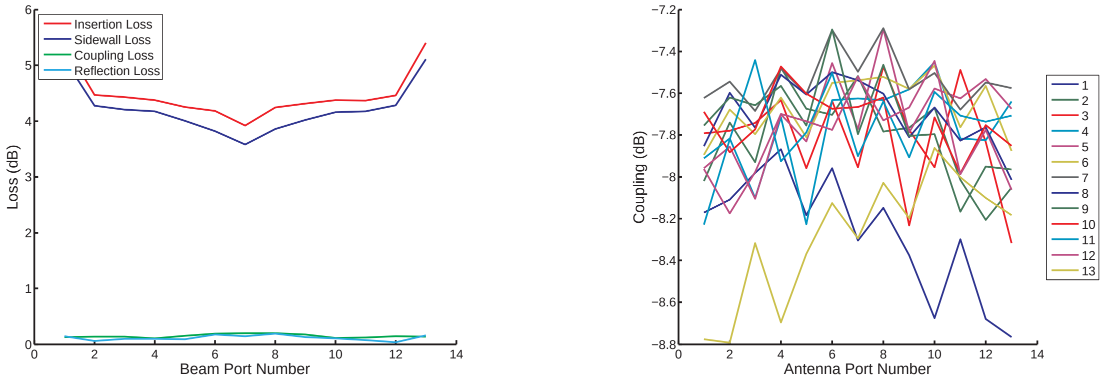

(a) Lens losses due to coupling, reflection, and dummy port absorbtion

(b) Excitation taper at the output for each beam port

Fig. 7.20: Single beam port performance. The simulated results show that the lens insertion loss will be dominated by energy lost to the sidewall of the lens. The antenna port excitation taper should be very linear except for the outermost ports.

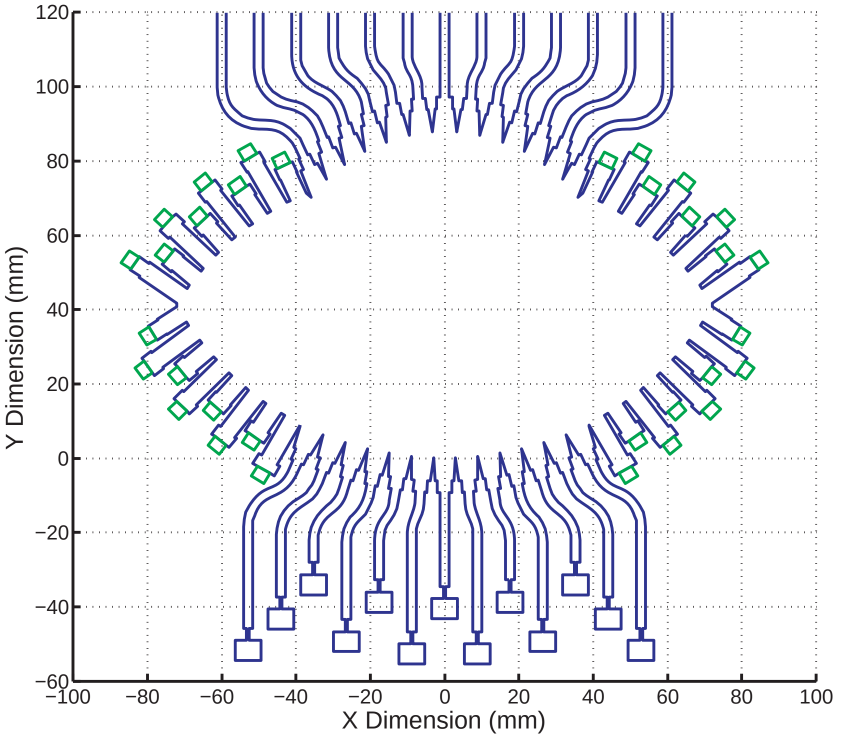

Figure 7.21: Single beam port Rotman lens. Early 17 GHz single port Rotman lens design.

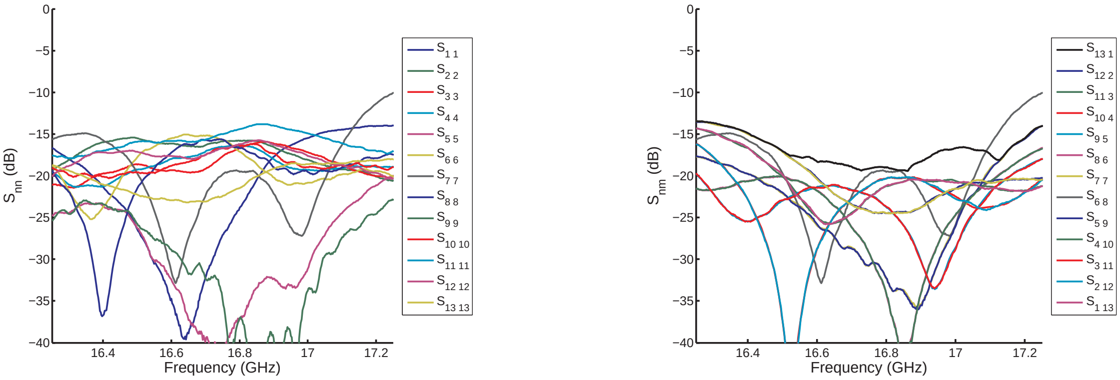

(a) Beam port reflection coefficients

(b) Beam port coupling

Fig. 7.22: Single beam port S-parameters. The reflection coefficients of the lens are very good, while beam port isolation is limited.

The reflection coefficients of this lens is shown in Figure 7.22(a). This lens implementation has demonstrated that a match of less than -10 dB is achievable for a 6 % bandwidth, consistent with that of the antenna element shown in Figure 7.18(b).

As shown in Section 7.2.2, the coupling loss is significant for single beam port lens designs. The other significant source of coupling loss is due to antenna mismatch. A wave excited from a given beam port propagates through the body of the lens to the antenna elements with a uniform phase gradient. The mismatch at each antenna element causes some of this energy to be reflected back with the same phase gradient. This causes increased coupling between mirror image beam ports. Figure 7.22(b) shows that coupling between mirrored ports is of the same magnitude as coupling between adjacent ports.

The beam pattern of each beam is seen in Figure 7.23(a). The sidelobe level of each beam is consistent with an almost uniformly excited antenna array. Closely spaced beam ports result in crossover points of the central beam of -1.15 dB, resulting in highly overlapped beams. The 3 dB field-of-view of 42° does not extend to the outermost beam port due to increased coupling of this beam port to the sidewalls of the lens. The performance of this lens implementation is summarised in Table 7.1.

Dual Sub-Port Rotman Lens

The following lens was developed to demonstrate the potential of multiple sub-port implementation of the Rotman lens. The specifications of this lens are identical to that of

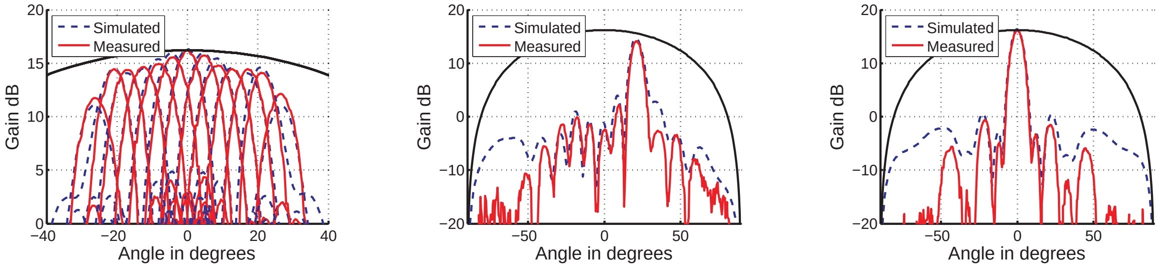

(a) Beam crossover (b) Outermost beam (c) Broadside beam

Fig. 7.23: Single beam port beam-forming performance. The beam-forming performance of the single port Rotman lens matches the expected simulated results and is consistent with a nearly linear array excitation. The measured and simulated beam patterns are shown in blue and red, with the expected maximum aperture gain in black.

Bandwidth : 16.25 GHz to 17.25 GHz
Field of View : 42°
Gain (Central Beam) : 16.4 dB
Crossover (Central Beam) : -1.15 dB
Sidelobes : 9.9 dB (12.9 dB Average)
Max Beam Port S_{nn} : -10 dB (-21 dB Average)
Min Beam Port Isolation S_{nm} : -13.5 dB (-27 dB Average)
Maximum Insertion Loss (Simulation) : 5.40 dB (4.47 dB Average)
Max Antenna Port S_{nn} (Simulation) : -12.6 dB (-14.4 dB Average)
Phase Errors (Simulation) : $< \pm 6^\circ$
Max Antenna Port Reflection (Simulation) : -12.6 dB (-14.4 dB Average)

Table 7.1: Early Rotman lens performance. Performance of the 17 GHz Rotman lens design shown in Figure 7.21.

the basic Rotman lens, described in Section 7.5.1, with the additional requirement of dual sub-ports.

The lens has been built using the same technique described in Section 7.5.1. Figures 7.24(a) and 7.24(b) show the body of the lens and the antenna ports, beam ports, and dummy ports, added before electromagnetic characterisation. The sub-ports on the focal plane are made narrower to better accommodate the 100 Ω line to which they will be matched.

The optimal port impedances are calculated and the impedance transformers, loads and antenna feed lines are added. Figure 7.24(c) shows the lens after the quarter wavelength transformers have been connected to the 3 dB power dividers of each beam port. The

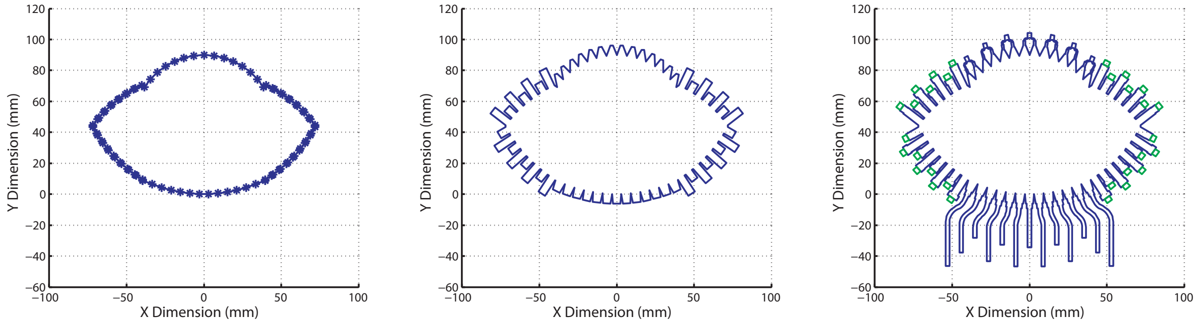

(a) Stage 1 (b) Stage 2 (c) Stage 3

Fig. 7.24: Double port lens build stages. The three lens layout stages are shown. Stage 1 defines the position of each beam port, stage 2 specifies the outer contour of the lens and is simulated to find the required port impedances. Stage 3 includes all impedance matching networks, dummy port loads and transmission lines.

phase of each sub-port is designed to minimise insertion loss by directing energy towards the antenna ports rather than the sidewalls of the lens.

Figures 7.25(a) and 7.25(b) show the expected loss of the lens, and the excitation taper of the array, for each beam port. As predicted in Section 7.1.4, the insertion loss of the dual sub-port implementation is considerably reduced when compared to the single port lens design. Comparing losses shown in Figures 7.20(a) and 7.25(a), an improvement of approximately 2 dB is achieved. The excitation tapering is readily apparent in Figure 7.25(b) and random fluctuations appear to be lessened. These attributes measurably reduce the strength of sidelobes of each beam pattern.

The final layout is prepared by tuning the length of each antenna meander line in the same way as the basic lens design. The completed lens is shown in Figure 7.26.

This lens has been characterised in the same way as the first design. A 2-port Wiltron 37369A VNA has been used to determine the 7 port scattering matrix of the lens. Unlike the single port implementation, coupling between adjacent beam ports does not dominate coupling loss. As explained in Section 7.2.2, the strongest coupling loss is between beam ports mirrored in the x-axis, and is attributed to antenna mismatch. The frequency dependance of this coupling loss, shown in Figure 7.27, closely matches that of the antenna element shown in Figure 7.18(b).

Section 7.2.2 showed that multiple sub-ports increase efficiency of the lens by reducing the energy lost to the sidewall of the lens. The antenna gain pattern shown in Figure 7.28(c) shows an increase in gain of the central beam to 18.2 dB, a 1.8 dB increase compared to

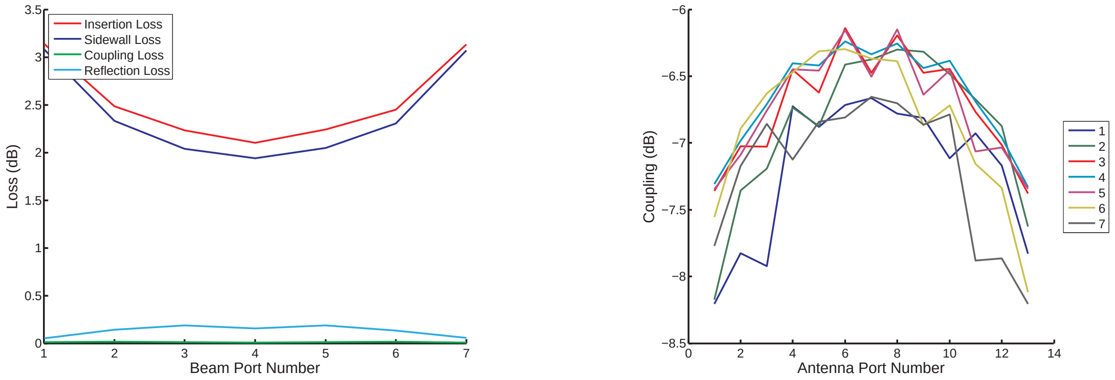

(a) Lens losses due to coupling, reflection, and dummy port absorbtion

(b) Excitation taper at the output for each beam port

Fig. 7.25: Double beam port performance. The simulated results show that while lens insertion loss is still dominated by energy lost to the sidewall of the lens, the dual sub-port has reduced these losses by 3 dB. As a result, the antenna port excitation taper is clearly no longer linear.

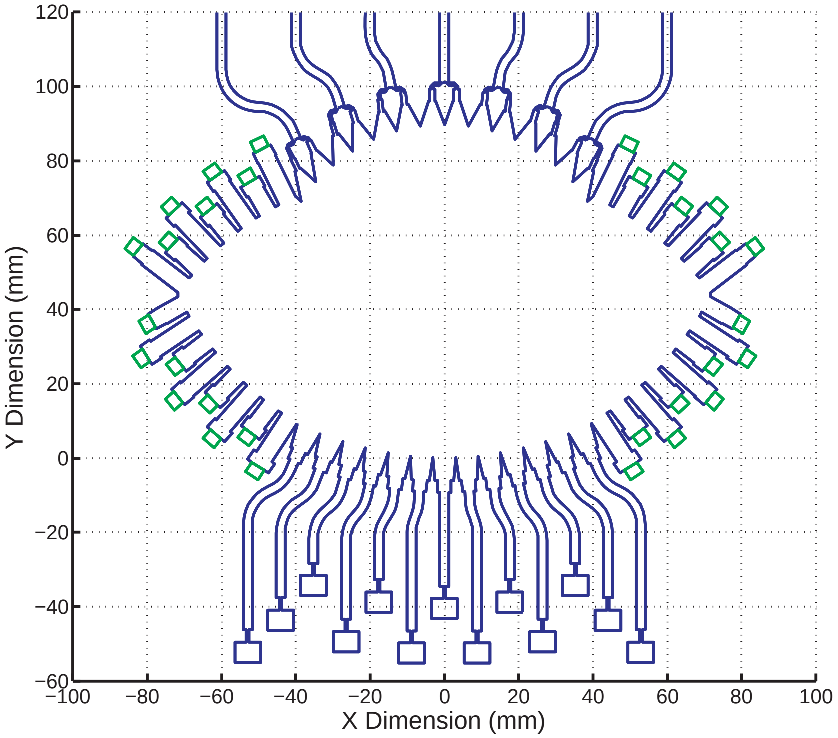

Figure 7.26: Rotman Lens. Early 17 GHz dual sub-port Rotman lens design.

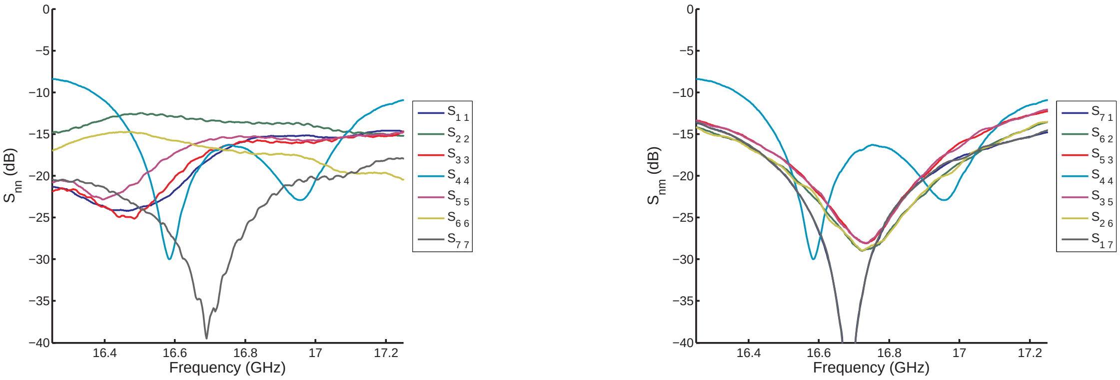

(a) Beam port reflection coefficient (b) Beam port coupling

Fig. 7.27: Rotman beam S-parameters. The reflection coefficients and beam port coupling are both improved. The frequency characteristic of the beam port coupling closely resembles the antenna reflection coefficient. This suggests that it is the antenna mismatch rather than the port coupling that is being seen here.

the basic lens design. Simulation predicts a decrease in insertion loss of 2.27 dB. The difference of 0.47 dB can easily be accounted for by the increase in beamwidth and the resulted reduction in gain due to the increased excitation taper of the double sub-port design.

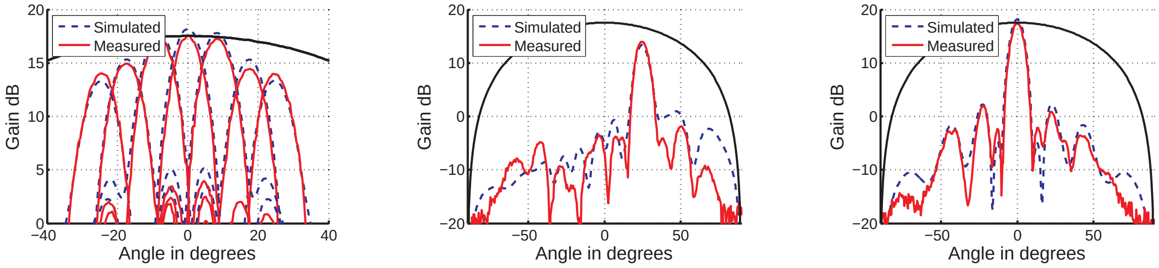

(a) Beam crossover (b) Outermost beam (c) Broadside beam

Fig. 7.28: Double beam port beam-forming performance. The beam-forming performance of the dual sub-port Rotman is consistent with the expected simulated results. The increased excitation taper has resulted in reduced sidelobe levels. The measured and simulated beam patterns are shown in blue and red, with the expected maximum aperture gain in black.

The capability to direct energy onto the antenna ports is clearly shown in the performance of the outermost beams. While the gain of the single port design drops off significantly for the outer beam ports, reducing the 3 dB field-of-view to 42°, the outermost beams of

Bandwidth	16.4 GHz to 17.25 GHz
Field of View	49°
Gain (Central Beam)	18.2 dB
Crossover (Central Beam)	-3 dB
Sidelobes	11.02 dB (14.5 dB Average)
Max Beam Port S_{nn}	-10 dB (-17.5 dB Average)
Beam Port Isolation S_{nm}	-10 dB (-30 dB Average)
Insertion Loss (Simulation)	3.14 dB (2.54 dB Average)
Max Antenna Port S_{nn} (Simulation)	-12.7 dB (-14.3 dB Average)
Phase Errors (Simulation)	$< \pm 5^\circ$
Max Antenna Port Reflection (Simulation)	-7.9 dB (-15.9 dB Average)

Table 7.2: Performance of the 17 GHz Rotman lens. Performance of the 17 GHz Rotman lens design shown in Figure 7.26.

this design do not suffer such degradation. This results in an increased 3 dB field-of-view of 49°. The excitation taper has improved the average sidelobe level by 1.6 dB.

Conclusions and Improvements

These designs demonstrate that the methods described in Sections 7.2 and 7.3 produce very effective lens designs across a narrow frequency band. Simulations using Ansoft Ensemble proved to be accurate in predicting both the scattering parameters of the lens and the resultant beam patterns. The matched loads used to implement dummy ports along the sidewall of the lens have been shown to be very effective at reducing reflections within the body of the lens.

The process used to characterise these lens designs could be improved significantly in two ways. The inclusion of the integrated antenna elements has limited the bandwidth over which the lens is characterised. Future lens designs should have antenna ports connected to measurable connectors rather than antenna elements. Further an extra simulation has been included in this design to account for variations in wavelength within the meander lines connecting the antenna ports to the array elements. This computationally expensive step is removed by properly characterising the circular microstrip line.

7.5.2 Broadband Rotman Lens

The mechanisms that limit the broadband performance of the Rotman lens have been discussed. This insight is now applied to the design and construction of a broadband Rotman lens. This lens is an attempt to achieve a bandwidth of 1:4, 5 GHz to 20 GHz, and a field-of-view of 40°. The only restriction imposed on this design is that the lens must achieve 3 dB beam cross over points at 10 GHz, for a practical linear array of antenna elements.

Array Description

Designing a scanned antenna array for operation across such a large bandwidth provides the same set of problems as the antenna ports of the lens. These problems are caused by interelement coupling resulting in varying input impedance with scan angle and frequency. Since the detailed design of an antenna array is beyond the scope of this thesis, the input to each antenna element is assumed to be equal to 50 Ω. This assumption is valid for an array of active antenna elements.

The position of each antenna port is derived from the position of the corresponding antenna element. Therefore, the interelement spacing is an important parameter for both the array and lens design. Increasing the antenna spacing of a linear antenna array beyond $\lambda/2$ introduces grating lobes as the main lobe angle increases, as described in Section 2.2.2. While the angular position of the beam is less than its grating lobe, decreasing the beamwidth of the antenna elements reduces the energy lost to the grating lobes. Therefore, the array element spacing is chosen so that there is no grating lobe within the systems field-of-view at the highest frequency of operation. The position of the first grating lobe is shown in Figure 7.29, for varying element spacing and main beam angle θ_0. A lens with a field-of-view of 40° has outermost beam angles of $\theta_0 = 70°, 110°$. These two beams will excite a grating lobe at $\theta_G \approx 131°$ and 49°, for an element spacing of λ. Therefore, an element spacing of λ, at the highest frequency of operation, is acceptable for a field-of-view of 40°.

Reducing element spacing below $\lambda/2$, at the lowest frequency of operation, increases coupling between elements and complicates antenna element matching in the same way it complicates antenna port matching. The lower limit is difficult to define without an in depth array design. However, it is safe to assume that element spacing below $\lambda/4$ is impractical.

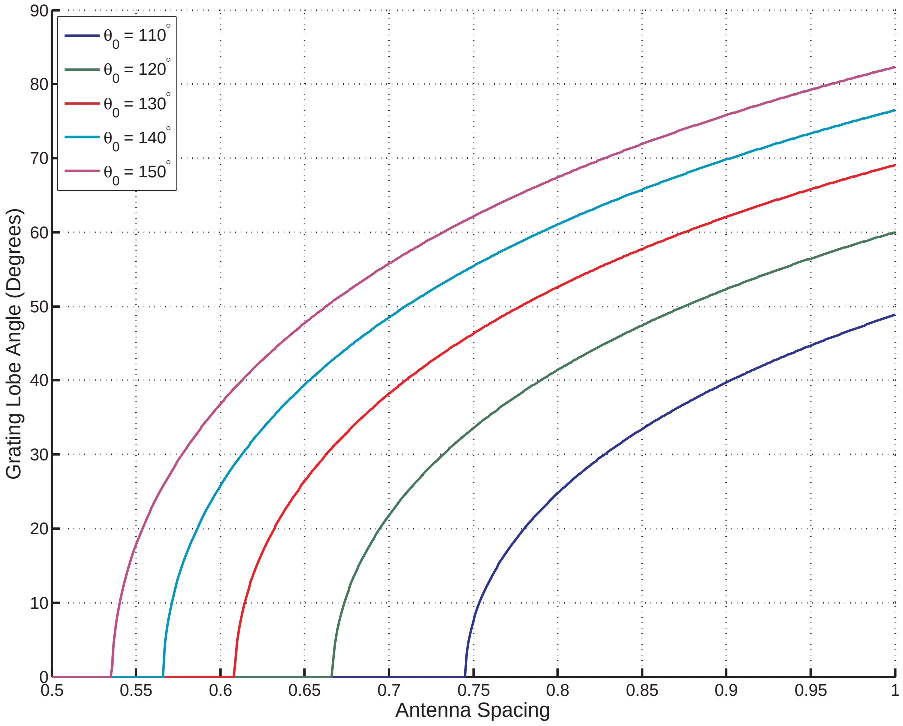

Figure 7.29: Element spacing and grating lobes. The antenna spacing should be chosen to exclude grating lobes from the field-of-view at the maximum beam angle. This figure shows the relation between grating lobe position and elements spacing. This is particularly important for a broadband lens design because the low frequency performance depends on maximising element spacing.

Substrate Choice

Section 7.1.5 demonstrated that the choice of a thick substrate simplifies port matching by reducing the imaginary component of the port impedance. Other considerations are cost, availability, and ease of manufacture. The high frequency laminate supplied by Rogers, RT/Duroid 5880, has been chosen as the lens substrate. The properties of RT/Duroid 5880 are shown in Table 7.3. Two materials have been considered to implement the dummy port loads on the substrate. Ohmega-Ply is the thin film impedance used in the early lens designs. While this is an ideal product for this application, it is no longer available in Australia. The only available alternative to Ohmega-Ply is Electrodag PR-406, a screen printed carbon polymer thick film resistive ink. This is unfortunate because the Electrodag PR-406 material is inferior to the Ohmega-Ply in the following ways:

- impedance per square tolerance,

Manufacturer	Rogers Corporation
Name	RT/Duroid 5880
Dielectric Constant	2.2
Loss Tangent	0.0009 at 10 GHz
Height	0.787 mm
Copper Cladding	35 μm
Impedance A	50 Ω/square Ohmega-Ply thin impedance film
Impedance B	10 Ω/square Electrodag PR-406 thick impedance film

Table 7.3: Lens Substrate. Substrate used to implement the broadband Rotman lens.

- edge tolerance,
- alignment tolerance and
- area required per load.

Lens Variables

The lens variables have been chosen to maximise the field-of-view, while maintaining an acceptable performance across the 5 GHz to 20 GHz band. The choice of α is based on the desired field-of-view of the lens, $\approx 2\beta$, and port spacing. Section 7.2.3 showed that as the field-of-view increases, the coupling loss between adjacent antenna ports becomes larger. Table 7.4 shows the magnitude of coupling loss taken from Figure 7.14. At the lowest frequency of operation, the magnitude of coupling loss increases to 3.7 dB for a field-of-view of 40°, and increases rapidly beyond that. Setting $\alpha < \beta$ to reduce coupling losses results in wider antenna ports and reduces the maximum operating frequency. Therefore, $\alpha = \beta$ is chosen resulting in antenna port spacing of approximately one wavelength at the highest frequency of operation.

The idealised performance of the Rotman lens far exceeds the performance of microstrip or stripline lens implementations for small to medium antenna arrays. Therefore, the geometry of a small to medium Rotman lens should be chosen to simplify construction rather than geometric aberration performance. The most important factors to consider when selecting the values of the Rotman variables are focal arc geometry, array arc geometry and port spacing. This is problematic because the impact of these choices cannot be gauged until the lens design is complete.

Maximum internal beam angle (α)						
Frequency	Antenna Port Coupling Loss (dB)					
f/f_0	0°	20°	40°	60°	80°	100°
0.5	0.01	0.5	3.7	15	27	30
1	0.01	0.3	0.5	1.1	2.7	5.5
2	0.01	0.1	0.3	0.4	0.4	0.5

Table 7.4: Antenna Port Coupling Loss. This table has been included to emphasise the relationship between frequency, beam angle, and coupling loss. The table demonstrates that the low frequency performance suffers as field-of-view increases. The results shown here are based on a linear array of twelve antenna ports with half wavelength spacing at f_0.

Section 7.1.5 demonstrated that beam ports must be constructed using multiple sub-ports for low loss, high bandwidth lens designs. To avoid the additional loss associated with overlapped beam ports, the size of the lens must be increased so that adjacent beams overlap at the 3 dB points. Figure 7.7 shows that a dual sub-port lens with a field-of-view of 20° should choose $f \approx 1.05$ to ensure 3 dB cross over.

The broadband lens performance is limited by the phase gradient between adjacent ports. Section 7.3.2 demonstrated that increased phase gradient lead to large port coupling and complicated impedance matching. To minimise the severity of these effects, the focal arc and antenna arc should face the opposite side of the lens as much a practical.

Figure 7.30 shows two possible choices of lens parameters. Figure 7.30(a) shows the beam port and antenna port positions for optimal g and Figure 7.30(b) shows the second local error minima for the refocused focal arc. Figure 7.30(a) shows an example of a good antenna arc while the arc in Figure 7.30(b) turns too far, almost pointing back on itself. The optimal g layout is chosen for this design.

Port Design

The discussion presented in Section 7.1 showed that the interface between the port and lens needs to be carefully considered to achieve an effective Rotman lens implementation. Table 7.5 presents the main sources of loss in relation to frequency, sub-port and feed network choice. The table shows that while using dual sub-port design reduces loss significantly at the lowest frequency, increasing the number of sub-ports to three does not reduce losses further due to additional complexity and losses within the feed network.

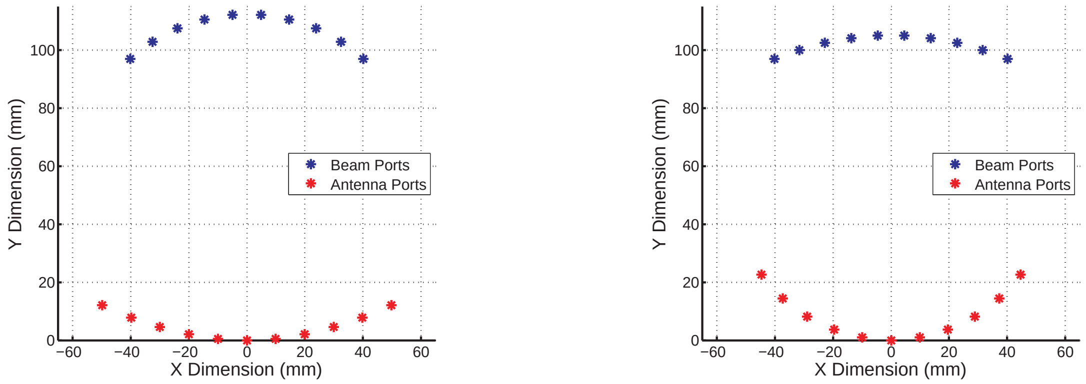

(a) $\alpha = 22.5°$, $f = 0.8333$, $g = 1.0635$ (b) $\alpha = 22.5°$, $f = 0.8333$, $g = 1.0026$

Fig. 7.30: Rotman lens variable selection. Subfigures (a) and (b) show the port positions of the optimal choice of g and the second local minima using a refocused focal arc described in Section 5.3. By comparing the two lenses, the optimal g results in a more consistent layout. This is because the ratio of g and f reduces the variation in beam port width and spacing, and the reduced curvature of the antenna arc improves illumination of the beam ports.

These losses are a result of neighbouring beam ports sharing sub-ports to maintain the 3 dB beam crossover point.

Electromagnetic simulation of a half wavelength wide microstrip line shows that propagation loss has a significant effect on the overall loss of the lens. Based on the loss of a wide microstrip line, the lens body is expected to experience an additional propagation loss, L_P, of:

$$\begin{aligned} L_P &\approx 1, 2.3, 4.1 \text{ dB/m}, \\ L_P &\approx 0.24, 0.54, 0.97 \text{ dBTotal}, \end{aligned}$$

at 5 GHz, 10 GHz, 20 GHz respectively.

Sections 7.2.2 and 7.3.1 explained that to realise such a broad bandwidth, the effective width of the beam ports must be greater than half the guided wavelength at the lowest frequency of operation. This is achieved by implementing beam ports using dual sub-ports and allowing individual port width to increase to one guided wavelength at the highest operating frequency.

Section 7.3.1 demonstrated that it is possible to keep the imaginary port impedance component small. Therefore, the use of the exponential impedance taper is appropriate for

Number of Sub-ports				
Frequency	Dummy Port Loss (dB)			
f/f_0	Single	Double	Triple	Taylor (3)
0.5	4.4	3.3	1.9	2.2
1	3.3	0.8	0.5	0.2
2	0.8	0.3	0.2	0.2
Frequency	Beam Port Coupling Loss (dB)			
f/f_0	Single	Double	Triple	Taylor (3)
0.5	3.5	1.3	0.5	0.5
1	0.6	0.11	0.06	0.03
2	0.01	0.01	0.01	0.01
	Feed Network Loss (dB)			
	Single	Double	Triple	Taylor (3)
	0	0	2.2	1.8
Frequency	Total Beam Port Loss (dB)			
f/f_0	Single	Double	Triple	Taylor (3)
0.5	7.4	4.6	4.6	4.5
1	3.9	0.9	2.7	2
2	0.8	0.3	2.4	2

Table 7.5: Source of Rotman lens losses. The insertion loss of the lens is the sum of the dummy port loss, port coupling loss and losses in the beam port feed network. This table shows how the number of sub-ports and the feed network effects these losses. The double sub-port solution has been chosen, for the focal arc of the broadband lens, to demonstrate its simplicity and performance. The dummy port loss is calculated using the two dimensional aperture model described in Section 4.3.1. The antenna ports are assumed to occupy $\pm 30^\circ$ and any energy radiation outside this is assumed to be absorbed by the dummy ports. The coupling loss is taken directly from Figure 7.14 and the feed network loss is calculated assuming ideal Wilkinson power dividers.

Antenna spacing	15 mm
Antenna port width	10 mm
Beam port width	10 mm
Field of view	40°
Beam positions	±20°, ±10°, 0°
Rotman variables	$\alpha = 22.5°$, $f = 0.8333$, $g = 1.0635$
Matching networks	Exponential taper
Antenna Port Phase Centre	1.5 mm
Beam Port Phase Centre	2.5 mm
Power dividing networks	-3 dB Power Divider or Wilkinson Divider

Table 7.6: Broadband Rotman lens body specification. Broadband Rotman lens body specification

port impedance matching. The Klopfenstein impedance taper offers improved performance compared to the exponential taper, but the author was not aware of it at the time of this design decision.

Section 7.1.3 explained the relationship between port position and aberrations, and how to reduce aberrations by placing the phase centre of each port or group of sub-ports at the port position described by geometrical optics. To establish the location of the beam port and antenna port phase centre, the two linear port arrays in Figures 7.31(a) and 7.31(c) are constructed and simulated using HFSS. The phase centre offset for the single antenna port, Figure 7.31(b), and dual sub-port beam port, Figure 7.31(c) are then calculated using Matlab.

Enough information has been gathered to define the specification of the lens body. This is given in Table 7.6. The lens body, shown in Figure 7.32(a), has been generated using Matlab and simulated using Ansoft Designer. The ideal real port impedance of the beam port sub-ports, antenna ports and dummy ports are calculated as described in Section 7.3. Simulation of the lens body using 1 GHz steps does not show any measurable performance improvement to warrant the additional complexity of a Wilkinson power divider at each beam port, instead a simple 3 dB power spitter has been used. Finally, ports, sub-port feed networks and dummy port loads are added along with the boundary of the substrate. The completed lens design is shown in Figure 7.33.

An aluminium housing has been designed to support the SMA connectors and protect the soft substrate during testing. The housing illustrated in Figure 7.34, consists of a solid aluminium base and wall, milled from a solid block, and two clamps. The clamps hold the

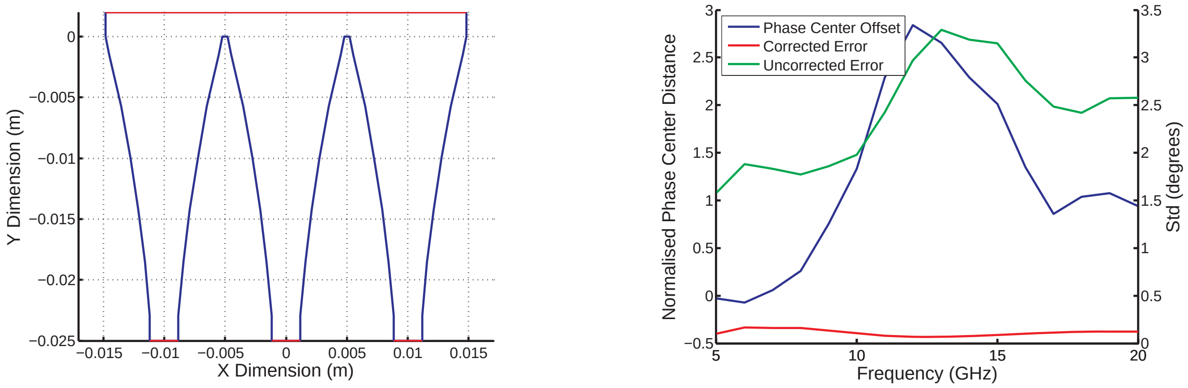

(a) Single port test structure (b) Single port phase centre

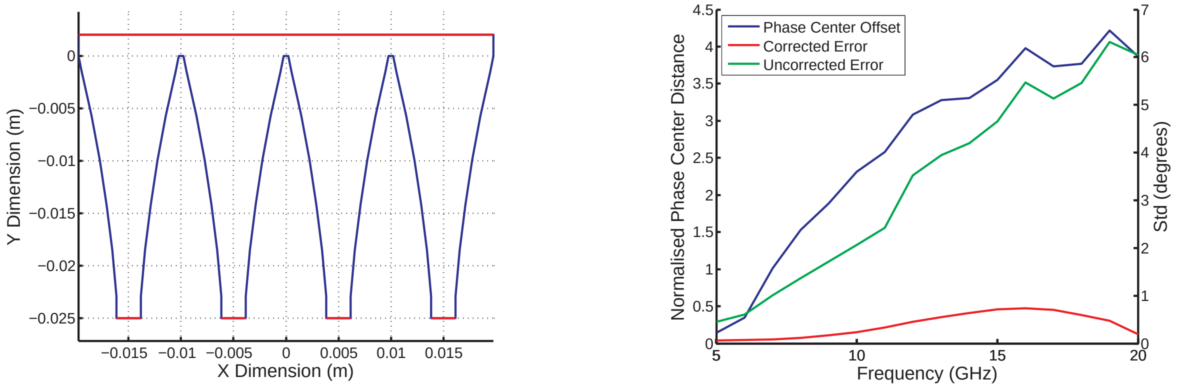

(c) Double-port test structure (d) Double-port phase centre

Fig. 7.31: Port phase centre. The phase centre of each port should be located at the positions defined by the Rotman equations. The phase centre is found using the electromagnetic models shown in Subfigures (a) and (c). The single port phase centre is found to be between 0.5 and 2 mm from the port interface, while the dual sub-port phase centre is found to be between 0 and 5 mm from the port interface. Subfigures (b) and (d) demonstrate that the improvement in phase error is considerable and becomes increasingly important as the number of sub-ports is increased.

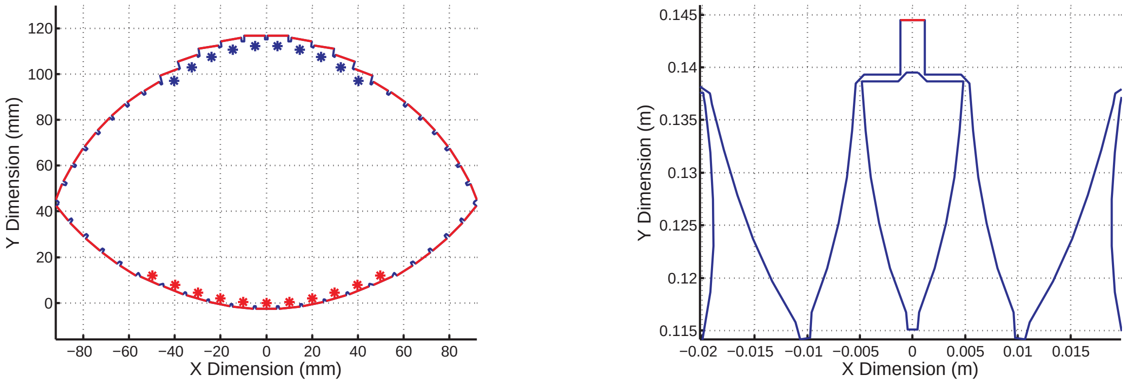

(a) Lens Body

(b) Dual sub-port feed network

Fig. 7.32: Broadband Rotman lens layout. The lens has been simulated in two steps. The first step characterises the body of the lens using the layout shown in Subfigure (a). The results of this simulation is used to design the ports, matching networks and resistive terminations. A beam port and feed network is shown in Subfigure (b). An additional simulation has been carried out to check to see if any significant performance advantage could be gained by using a Wilkinson power divider instead of a 3 dB power divider. The results showed that the additional complexity and loss would not result in any measurable performance improvement.

substrate to the base, ensuring a good electrical contact between the ground plane of the substrate and the aluminium base. A photo of the final lens can be seen in Figure 7.35.

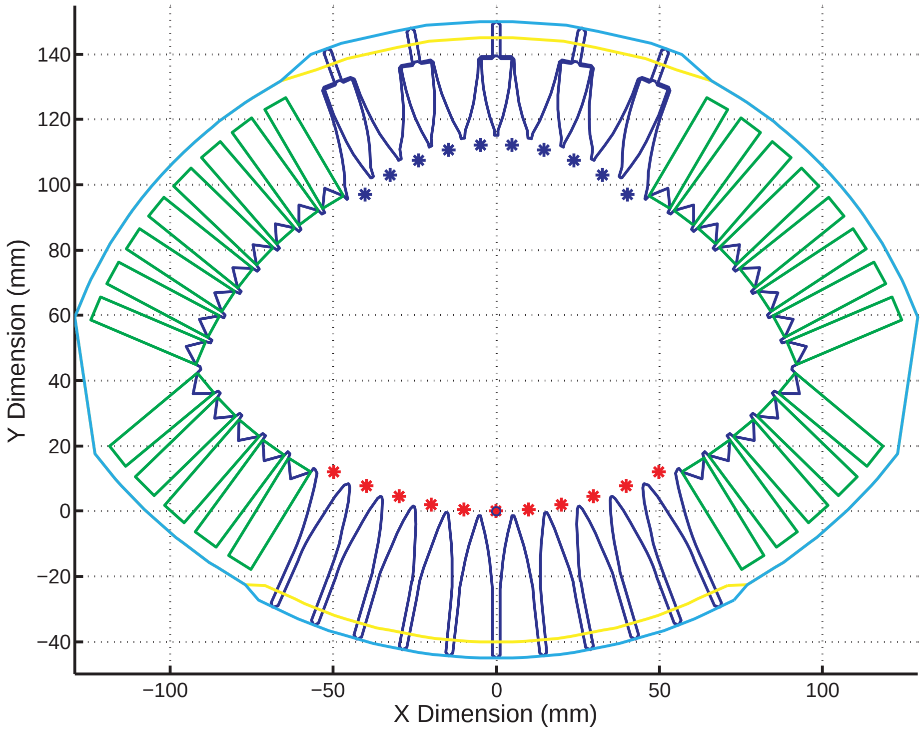

Figure 7.33: Completed broadband Rotman lens layout. The completed lens design is shown here. The dummy port loads, beam and antenna ports, and sub-port feed network have been added to the layout. The cyan line defines the substrate periphery while the green lines define the thick film impedance and the blue line the copper foil.

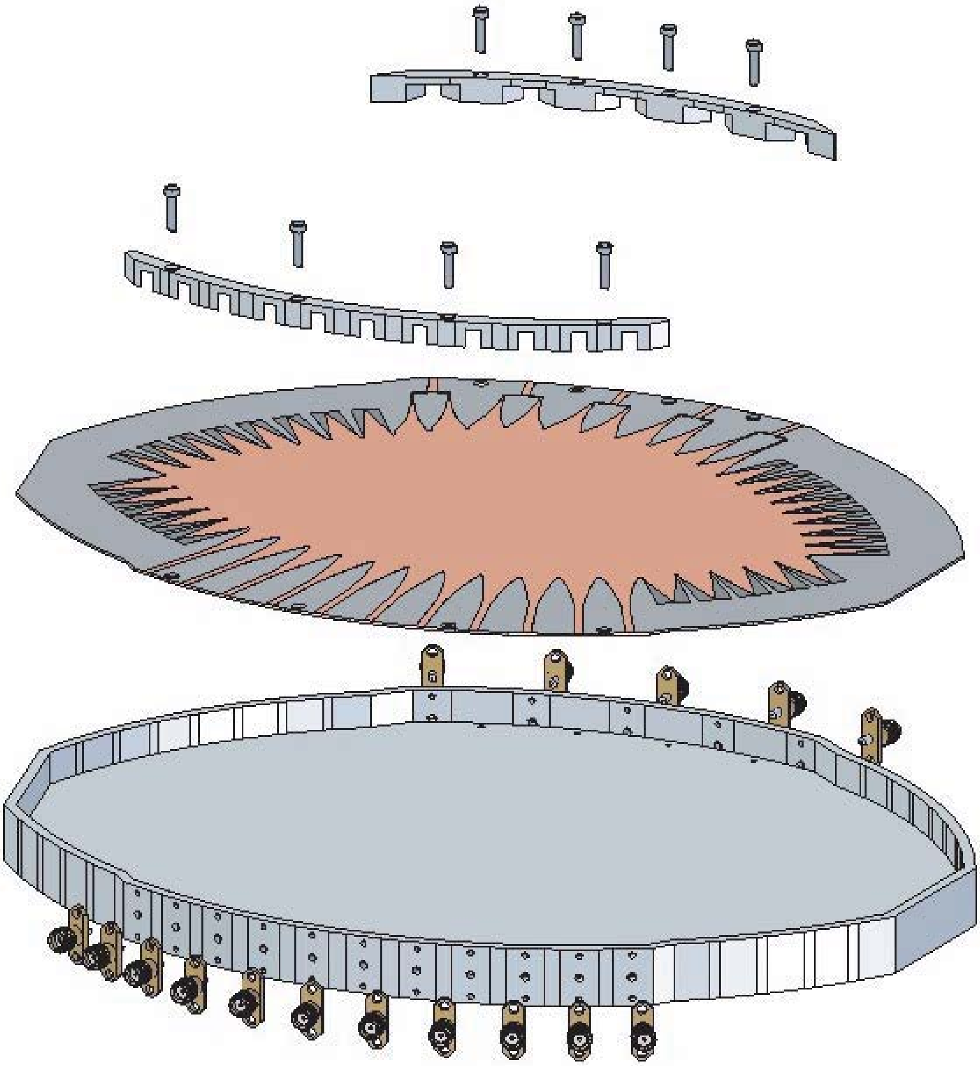

Figure 7.34: Lens housing. The Duroid substrate does not have significant mechanical strength so an aluminium housing has been constructed. The housing consists of the base that supports the SMA connectors and substrate, and two clamps that ensure a good conductive connection between the lens ground plane and the housing.

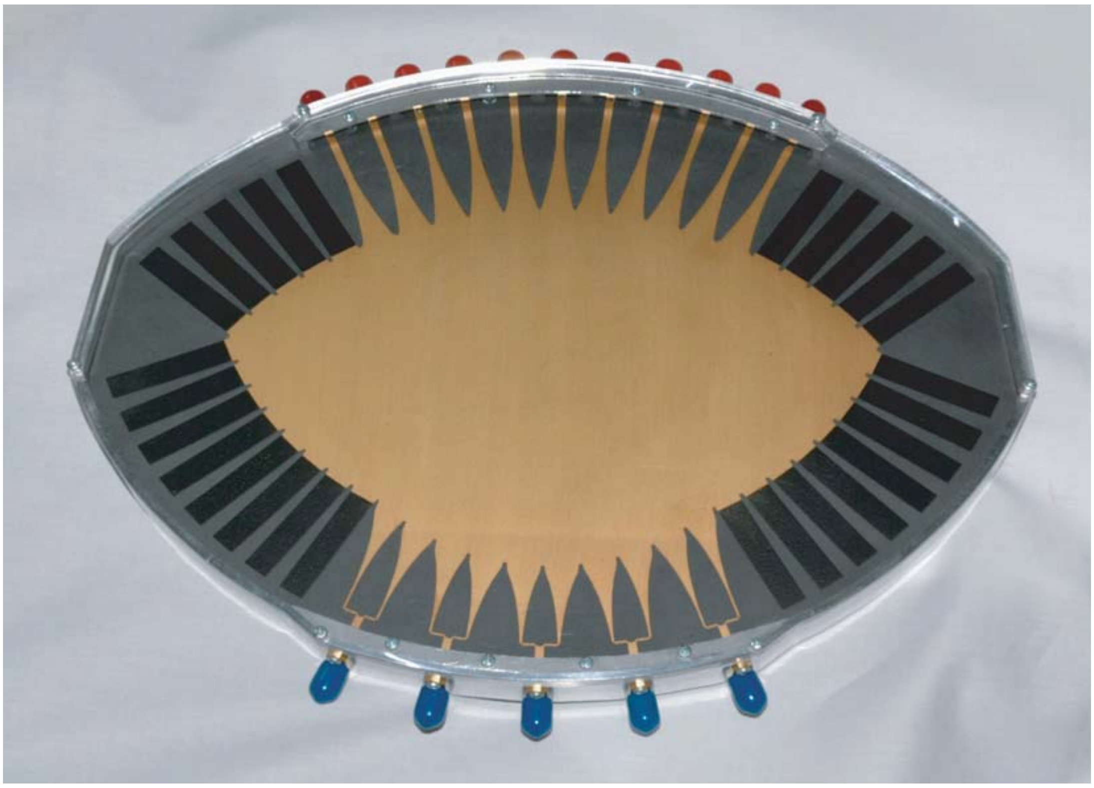

Figure 7.35: Broadband Rotman lens. The fabricated lens is shown here. The five blue SMA caps are the beam ports and the eleven red caps are the antenna ports. The black rectangles are the dummy port loads, made using Electrodag PR-406 thick film carbon paste.

Simulated and Measured Results

The lens design shown in Figure 7.35 has been manufactured and measured using a four port vector network analyser from 1 GHz to 41 GHz with a resolution of 50 MHz. The thirty five four port S-parameter measurement have been combined into a sixteen port S-parameter set and compared to the simulated results. The measured results made it apparent that the simulated frequency resolution of 1 GHz, used to design the lens, is insufficient to see all the properties of a layout of these dimensions. Therefore the lens design has been simulated again with a frequency resolution of 0.1 GHz.

The reflection coefficient of each port has been displayed in Figure 7.36. The antenna port reflection coefficient is not expected to remain below -10 dB because only single antenna ports are being excited. The reflection coefficient of the antenna ports demonstrates a poor match between measured, Figure 7.36(a), and simulated results, Figure 7.36(b). Similarly, the beam ports simulated and measured S_{nn} do not match well. This is not unusual because the simulated reflection coefficient does not include microstrip to coaxial transition. Further, the reflection coefficient is reasonably small, allowing small differences between the simulation model and measured structure to cause large variation between the two results. With the exception of beam port 3, the beam ports maintain match of <-10 dB above 5 GHz. In contrast, the measured reflection coefficient of beam port 3 reveals regularly spaced nulls and peaks in the frequency response. This frequency response is indicative of a significant reflection located a large distance from the input of beam port 3.

To examine the source of the frequency domain ripple of beam port 3, the time domain response of the lens has been calculated. This is carried out by calculating the inverse Fourier transform of the measured frequency response. The time axis of Figure 7.37 has been converted to distance using the relation $d = ct/\sqrt{\varepsilon_r}$ for port coupling and $d = 0.5ct/\sqrt{\varepsilon_r}$ for port reflection, where c is the speed of light, t is time, and the relative dielectric constant ε_r is 2.2.

Figure 7.37 shows the time domain response reflection coefficient of beam port 1 and 2, and the coupling response of the central antenna and beam ports, 6 and 3 respectively. The red and blue time domain responses of beam ports 1 and 3 shows a large peak, 3 mm from the input reference plane. This distance corresponds to the coaxial to microstrip junction and has been checked using an open circuit SMA connector. The large green peak 202 mm from the input reference plane of beam port 3 is the output reference plane of antenna port 6. Beam port 3 experiences an additional reflection from 3 mm inside the

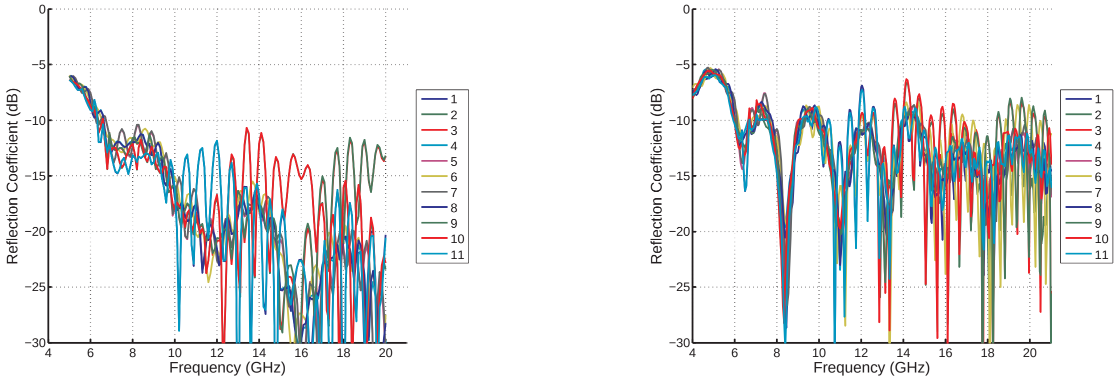

(a) Simulated Antenna Port (S_{nn}) (b) Measured Antenna Port (S_{nn})

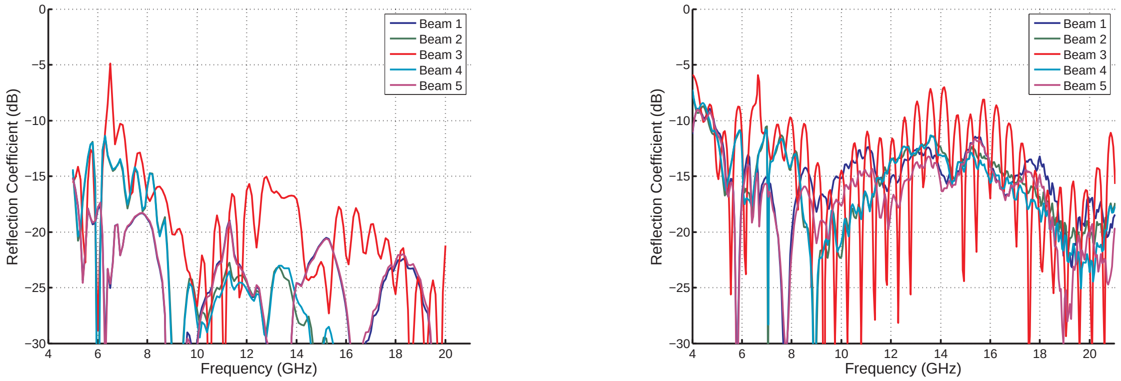

(c) Simulated Beam Port (S_{nn}) (d) Measured Beam Port (S_{nn})

Fig. 7.36: Measured and simulated reflection coefficient. The simulated reflection coefficient of the beam and antenna ports, Subfigures (a) and (c), are a poor match to the measured results, Subfigures (b) and (d). Beam port three also shows regular pattern of nulls in the reflection coefficient is due to the interface between the antenna port microstrip lines and SMA connector.

antenna port output reference plane, corresponding to the microstrip to coaxial transition, and an increased reflection from 13 mm inside the lens, caused by the 3 dB power splitter. The *Time Gating* facility of the network analyser has been used to remove the effect of the second time domain peak of beam port 3. This confirms that it is the second peak, not the first peak that is responsible for the frequency domain ripples of beam port 3. Therefore, the poor reflection coefficient performance is caused by the microstrip to coaxial junction rather than the Rotman lens geometry.

The simulated and measured losses match very closely as seen in Figure 7.38. The insertion loss of a well designed and matched lens is dominated by the lens loss as can be seen by

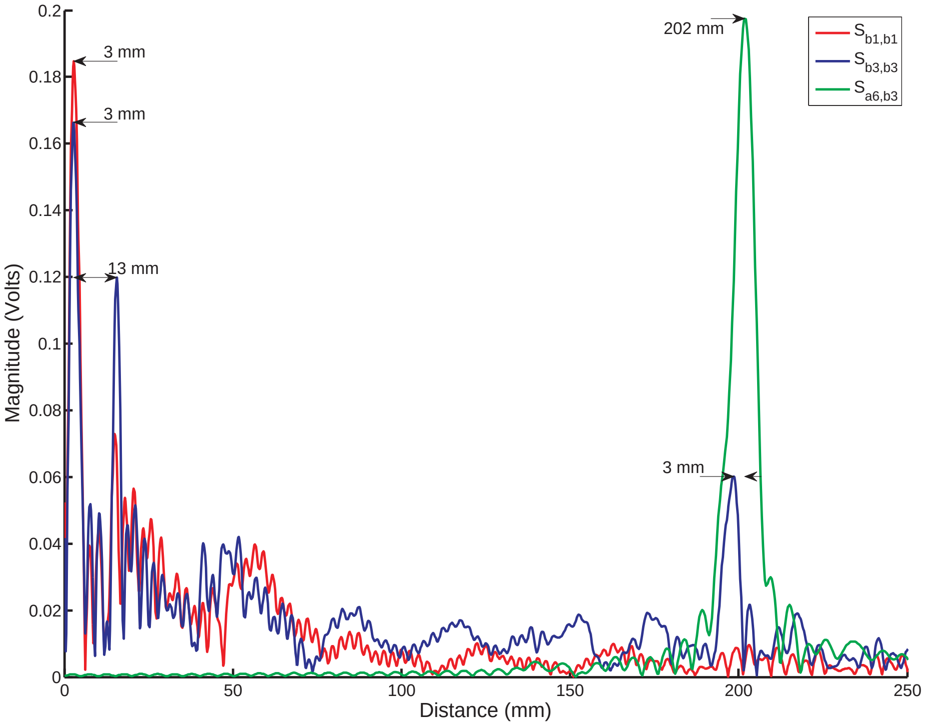

Figure 7.37: Measured time domain response. The position of the reflection causing the regular nulls and increased reflection coefficient of beam port 3 has been determined by examining the time domain response. The time domain response has been generated by calculating the inverse Fourier transform of the measured S-parameters. The x-axis is shown in units of distance by converting time to the distance electromagnetic energy could travel through a medium with a dielectric constant of 2.2. The discontinuity between microstrip and coax has been measured to be 3 mm using an unconnected SMA connector. An additional peak is seen in the time domain response of beam port 3, 3 mm short of the $S_{a6,b3}$ response. When this peak is time gated out, the reflection coefficient resembles the simulated response.

comparing the magnitudes of total insertion loss, Figures 7.38(a) and 7.38(b), and dummy port loss, Figures 7.38(c) and 7.38(d). The lens loss is a combination of dummy port loss, metal loss, and substrate loss. Losses due to coupling to the dummy ports should reduce as frequency increases, causing the gain of the beam ports to increase. As the frequency increases, ohmic loss increases, as the skin depth decreases, and substrate loss increases. These trends are clearly shown by Figure 7.38, however, there are also two unexpected features present. Figures 7.38(a) to 7.38(d) all show a 1 to 2 dB increase in loss at 14 GHz and the measured results show signs of a disturbance between 6 and 7 GHz.

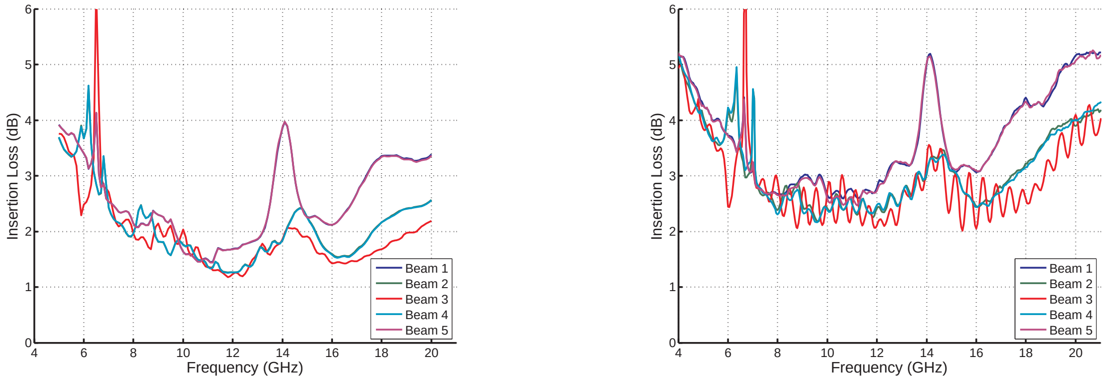

(a) Simulated Insertion Loss (b) Measured Insertion Loss

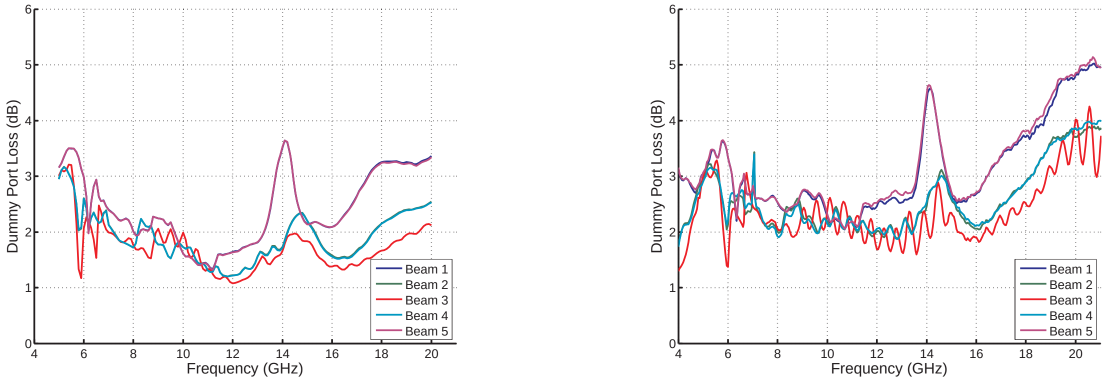

(c) Simulated Dummy Port Loss (d) Measured Dummy Port Loss

Fig. 7.38: Measured and simulated insertion and dummy port loss. The simulated insertion and dummy port loss are a very good match with the measured results. The measured results show that the lens has 0.5 dB to 1 dB more loss than the simulation predicted. Both simulated and measured results show a local increase in loss at around 14 GHz, however, the poor resolution of the simulated results did not show the narrow-band disturbance between 6 and 7 GHz.

The origin of the 6 to 7 GHz disturbance is found by examining the return and coupling loss in Figure 7.39. The disturbance is clearly seen in Figure 7.39(d) but less so in the other plots. Therefore it is probable that the disturbance is a direct result of coupling between the neighbouring port structures. This has been confirmed by viewing the simulated surface currents at these frequencies. These frequencies couple to an odd mode in the dual sub-ports, causing increased reflection coefficient and losses to the dummy ports. This effect could be removed from the frequency range of the lens by increasing the length of each sub-port or using a Wilkinson power divider instead of the simpler 3 dB power divider.

The peak in loss at 14 GHz is much more difficult to explain. Figure 7.39(c) shows a similar peak, suggesting that the two dimensional beam pattern is being disturbed by a subtle coupling between sub-ports. Examination of current distributions within the body of the lens shows no obvious problem.

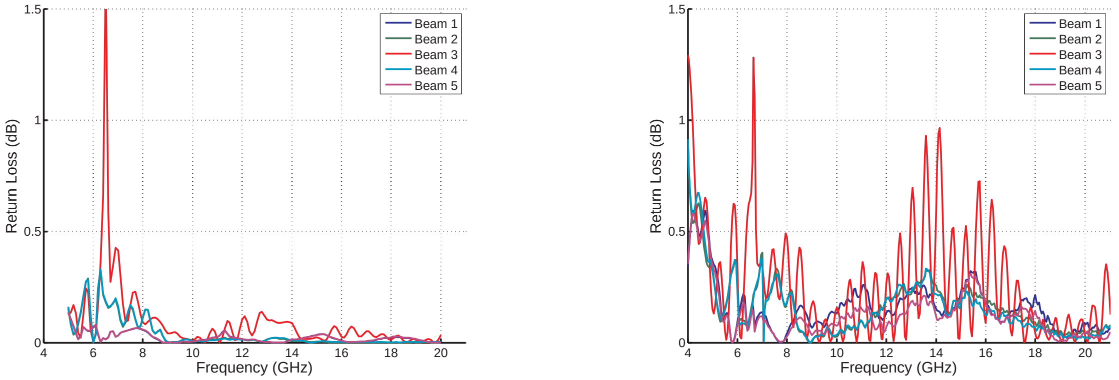

(a) Simulated Reflection Loss

(b) Measured Reflection Loss

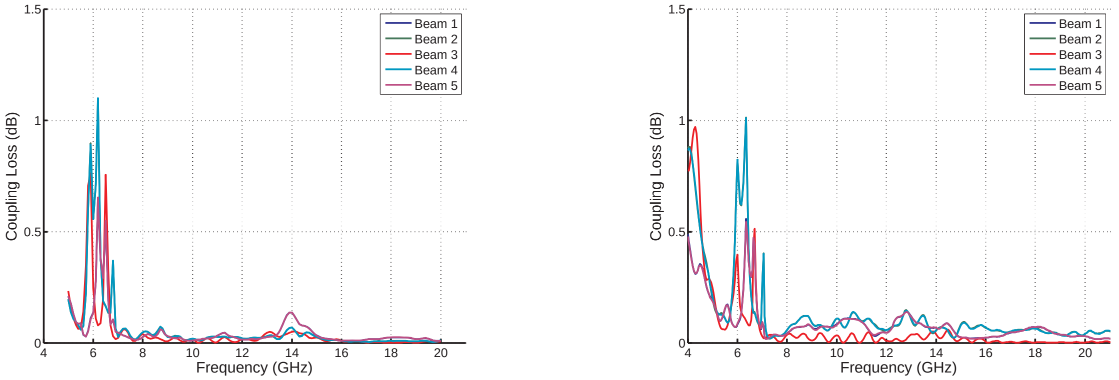

(c) Simulated Coupling Loss

(d) Measured Coupling Loss

Fig. 7.39: Measured and simulated return and coupling loss. The simulated beam port reflection loss appears to match the measured data well except for the regularly spaced nulls of beam port 3. The simulated and measured coupling loss are also a good match. Subfigures (b) and (d) clearly show that the disturbance between 6 and 7 GHz is a result of beam port coupling.

This Rotman lens is designed to drive a broadband linear array. To show the beamforming performance of the lens across this bandwidth, a contour plot has been used. Figure 7.40 shows the array factor of the first three beam ports, calculated using the measured results and defined in Section 2.2.2. The 6 to 7 GHz disturbance is visible in all three graphs and the grating lobe can be seen in Figures 7.40(a) and 7.40(b) at higher frequencies.

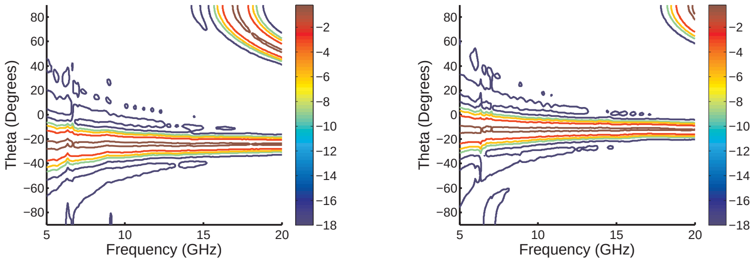

(a) Array Factor Gain, Beam 1 (b) Array Factor Gain, Beam 2 (c) Array Factor Gain, Beam 3

Fig. 7.40: Measured array factor gain. To display the array factor of the theoretical array driven by this lens, a contour plot has been generated for each beam port relating the beam angle, theta, and frequency. The contour plots show the presence of the grating lobe in Subfigures (a) and (b) due to the wide antenna spacing. The disturbance between 6 and 7 GHz can be seen as a narrow gap in the ridge of the main beam in Subfigure (c).

The phase error associated with each beam has been presented in Figure 7.41. Like the simulated results, the measured RMS phase error increases with frequency and is approximately the same magnitude. The 6 to 7 GHz disturbance is causing large phase errors explaining the poor beam-forming performance in this frequency range.

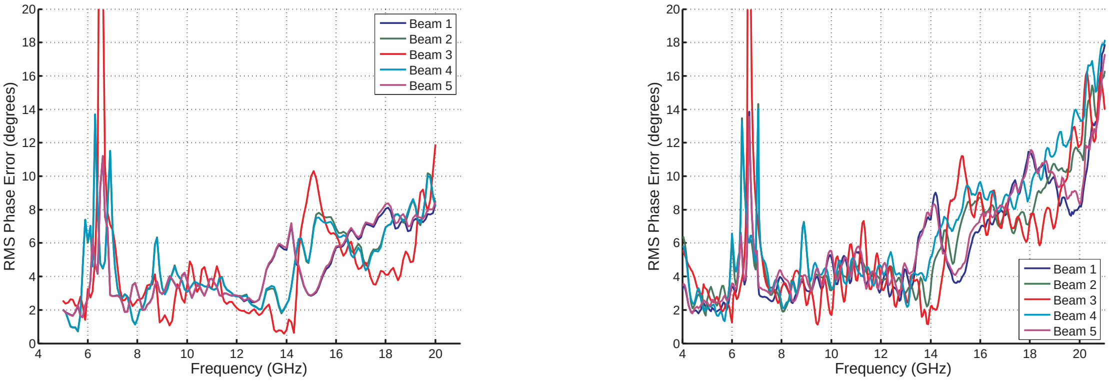

(a) Simulated Phase Error (b) Measured Phase Error

Fig. 7.41: Measured and simulated phase error. The measured phase error is approximately 1.5 times larger than predicted by simulation. The higher resolution of the measured results shows that the 6 to 7 GHz disturbance has a detrimental effect on phase error as could be seen in Figure 7.40.

The time domain response of the first three beams has been calculated to gain insight into the cause of the phase errors. Figures 7.42(a) to 7.42(c) show that the Rotman lens exhibits a good impulse response. The outermost antenna ports suffer from a multi-path component resulting in a second small peak less than 10 mm from the main peak. The small difference in distance suggests that the two paths are close to one another. The second peak becomes larger for the outer beam ports and antenna element with the largest delay, suggesting that the additional peak may be caused by a reflection from the array arc or neighbouring beam port.

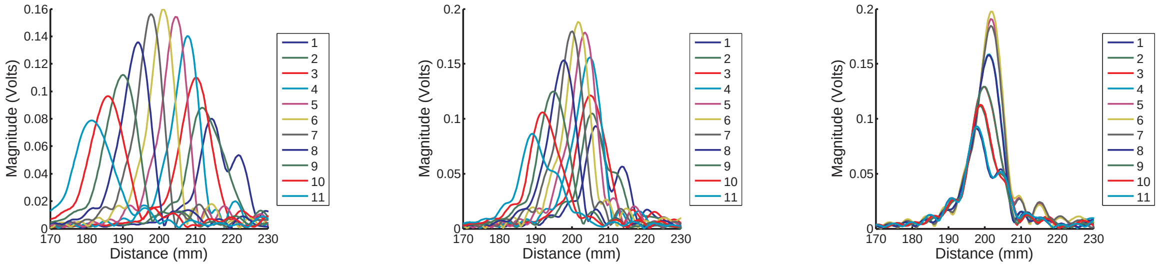

(a) Beam 1 (b) Beam 2 (c) Beam 3

Fig. 7.42: Measured array time domain response. The impulse response of each beam port of the Rotman lens is shown here. The excitation tapering across the array aperture is visible. The double peak of the outer antenna ports may be a further symptom of the 6 to 7 GHz disturbance.

The quality of the beam port isolation is related to both the coupling between the beam ports and the quality of the impedance match of the antenna ports and transmission lines. Lenses using multiple sub-ports, to construct each beam port, are able to achieve very low coupling between beam ports. Under these circumstances the beam port isolation is limited by the energy reflected form the antenna ports, transmission lines and connectors. While beam port coupling is strongest between adjacent ports, coupling due to reflection is largest between ports that are symmetrically placed on the lens axis. The simulated and measured beam port isolation is shown in Figure 7.43. The measured data clearly shows both forms of coupling that limit the beam port isolation. The red and blue lines that steadily drop with frequency are a result of direct coupling. The relatively flat blue and cyan lines are caused by reflections from the microstrip to coaxial transition. The beam port isolation is limited by the reflection coefficient of any component or system connected to the output of the lens.

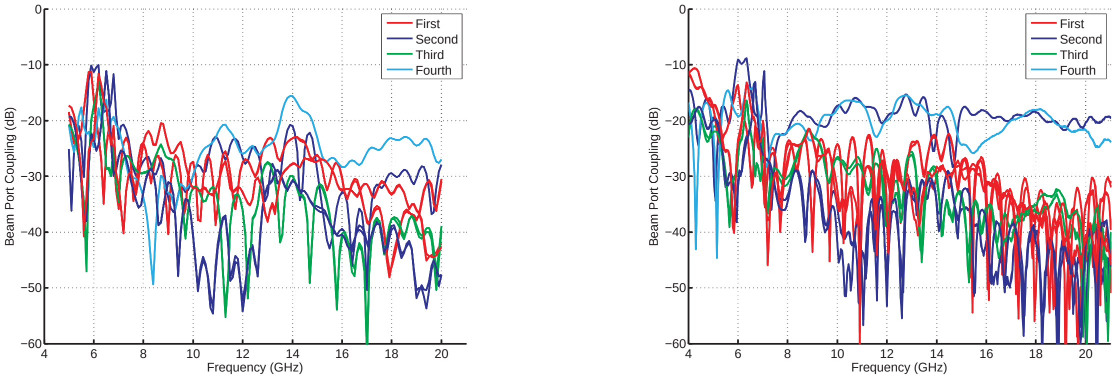

(a) Simulated Beam Port Coupling

(b) Measured Beam Port Coupling

Fig. 7.43: Beam port coupling. The magnitude of the simulated beam port coupling appears consistent with the measured results, with the exception of two lines. These lines represent the coupling between beam ports 1 and 5 and beam ports 2 and 4. This increase in coupling is also due to the additional reflection from the microstrip to coax interface.

Summary

This broadband Rotman lens design is an attempt to achieve a 1:4 bandwidth and field-of-view of 40°. While the field-of-view target has been successful, the bandwidth has been limited to 3:1 by electromagnetic interactions between the ports on the focal arc. The solution to this problem may be as simple as increasing the length of the exponential impedance taper or replacing the 3 dB power splitter with the Wilkinson divider. The focusing ability of the Rotman lens has been highlighted by the frequency domain ripple present on the reflection coefficient of beam port 3. This ripple is caused by the in phase addition of the reflections from each antenna port microstrip to coax transition. The magnitude of the beam port isolation has also been limited by the performance of the housing and microstrip to coaxial transition.

The Rotman lens design procedure could be improved further by increasing the simulation frequency resolution, enabling some geometry problems to be detected and addressed earlier. The use of Ohmega-Ply thin film impedance to implement both dummy port loads and Wilkinson power dividers, at each beam port, may increase the immunity of the lens to focal arc port interactions. This is because the Wilkinson power dividers absorb the odd mode excitation of dual sub-ports rather than reflecting the energy back into the body of the lens. Finally, the manufacturing tolerance of the lens housing and quality of the SMA connectors could be improved, in doing so removing some of the performance limitations imposed on the lens design.

The broadband Rotman lens has demonstrated the effectiveness of the port design and matching techniques described in Section 7.3. The links between insertion loss, lens loss, coupling loss, reflection loss, frequency and field-of-view has been clearly described and demonstrated. Most importantly, this work has moved the focus away from the optimisation of the theoretical geometrical Rotman lens and onto the electromagnetic interactions between the port geometry and lens body.

7.6 Chapter Summary

Despite the abundance of Rotman lens examples in the literature, there is surprisingly little work examining the fundamental limitations of the microstrip Rotman lens. To address this gap in knowledge, the microstrip port to parallel plate interface has been explored. Electromagnetic simulation of the port–lens interface has clearly demonstrated the effectiveness of port pointing, and the treatment of ports as two dimensional antenna elements. These simulations have also demonstrated that ports will operate effectively while supporting higher order modes. This work has shown that second order modes will only be strongly excited by energy reflected from the sidewall of the lens. Therefore, a well designed lens sidewall will allow port widths to be increased to almost one wavelength wide without any performance penalty.

Finally, this work has shown that the accepted practice of placing the port–lens junction at the port position described by the Rotman equations will result in phase errors an order of magnitude above those predicted by geometrical optics. This has highlighted the need for a thorough understanding of the Rotman lens port geometry if a high performance lens is desired.

While the treatment of the microstrip port as a two dimensional antenna element is relatively intuitive for a correctly matched port, achieving a good match is not a trivial task. This work has shown that the port impedance is not only effected by the proximity of neighbouring ports, but also port type. The impedance matching method must correctly account for the mutual coupling between elements and the relative excitations. This chapter has developed a matching technique that achieves this goal. This has been applied to matching the single beam port, the multiple sub-port beam port, and the antenna port array. How this method should be applied to determine the dummy port loads has also been discussed.

The techniques developed in this thesis produce a lens with well-dimensioned and correctly placed ports that have been efficiently matched to the input and output transmission lines of the lens. It is only now that the true limitations of the microstrip based Rotman lens become apparent. While a narrow-band lens is a relatively simple problem to optimise, the broadband lens is limited by the mutual coupling between both beam ports and antenna ports. This work has demonstrated that the seriousness of these effects can be reduced by constructing beam ports using multiple sub-ports. However, the performance of the antenna port array is degraded as the field-of-view increases. While the impedance matching techniques address the effects of antenna port coupling, the varying phase gradient makes an ideal solution impossible.

To achieve low aberration levels, the sidewalls of the Rotman lens must be designed to absorb any incident radiation to prevent this energy reflecting back into the lens and degrading the lens performance. The lenses described in this chapter use dummy ports terminated using a planar, thin film impedance load. The operation of this novel microstrip impedance termination has been described. Three examples have been used to demonstrate how this approach is capable of producing both narrow-band and broadband loads using a range of impedance films.

This chapter concludes by applying the insight gained in this thesis to the design of three Rotman lenses. The first two lenses are narrow-band lenses constructed with an integrated antenna array. These early lens designs show the relative performance of single and double port lens implementation. In an attempt to produce a lens at the theoretical limit of lens performance, a 1:4 bandwidth, 40° field-of-view, Rotman lens design has been attempted. While unforseen interactions between the beam port feed networks has limited the low frequency performance, this lens design has demonstrated a 7 to 20 GHz bandwidth. This lens represents the current state-of-the-art in Rotman lens design.

Chapter 8

Conclusions and Recommendations

THIS chapter draws together the conclusions from the work described in this thesis, and highlights a number of novel contributions to the analysis, design and construction of monolithic Rotman lenses. This chapter concludes this thesis by discussing directions for further research in this domain.

8.1 Introduction

The research conducted in this thesis is summarised in Section 8.2. This is followed by Section 8.3, where areas that require additional development, or where the Rotman lens may be applied in a new way, are discussed. Section 8.4 then summarises the major conclusions and novel contributions of this work.

8.2 Thesis Summary

This research has advanced monolithic constrained lens design and construction in two distinct ways. The first of these targeted the optimisation of the Rotman equations in the role as a feed network for a linear antenna array. The second focused on the physical implementation of microstrip or stripline constrained lenses. Perhaps the most useful outcome of this work is a clearer understanding of the performance limitations of monolithic constrained lenses and the mechanisms that are responsible. These areas are further elaborated below.

8.2.1 Theory of Rotman Lens

Chapter 2 introduces the basic principles of antenna elements and their performance in an array and concludes by introducing the Rotman lens. Section 4.2 presents the Rotman equations and the popular methods used to select an optimal variable set for a given application. Chapter 5 takes a fresh look at these methods and sets about presenting the Rotman equations in a form that is better suited to the application of a linear antenna array feed network.

The original equations presented by Rotman and Turner (1963) are normalised to the focal length of the two outer focal points. Therefore, the lens must be first scaled by the size of the aperture before intelligent comparison can be made with another lens using different variable values. Section 5.1 has presented these equations normalised by aperture size, instead of focal length, allowing two sets of lens variables to be compared directly.

The accepted method, used in the literature, to evaluate the aberration performance of a particular set of Rotman variable values does not closely relate to the expected beam-forming performance of the lens. Section 5.2 examines two types of phase error, linear phase error, and non-linear phase error. Linear phase error causes a shift in the angle of the beam's maximum but does not degrade the quality of the pattern. The non-linear phase errors are responsible for increased beam width and sidelobes, and reduced peak gain. Instead of measuring the non-linear errors by the magnitude of the maximum deviation from ideal, as encouraged by the literature, the strength of the aberrations is recorded as the RMS phase error. This measure bears a much closer relationship to the resultant degradation of the beam pattern.

With a convenient form of the Rotman equations and a sensible measure of lens aberrations, the remainder of Chapter 5 is devoted to addressing the extensive discussion in the literature regarding the optimal selection of Rotman variable values and focal arc shape. In contrast to the conclusions presented in the literature, numerical optimisation of the Rotman variables and focal arc clearly demonstrates that the circular focal arc achieves very nearly optimal performance. The optimal focal arc, found using refocusing, is unable to achieve any significant improvement in aberrations. The unexpected result of this analysis is the discovery that the refocused focal arc is able to produce a significant reduction in lens size without a large increase in phase error.

The circular and refocused focal arcs have been compared with the performance of the symmetrical Rotman lens. Before this could be done, new equations for the symmetrical Rotman lens had to be derived. Again, in contrast to opinions expressed in the literature, the circular focal arc is superior in every respect.

8.2.2 Implementation of Constrained Lens

Section 4.3 reviewed the tools and methods that have been developed to construct the microstrip and stripline Rotman lenses presented in the literature. A comprehensive study of the port to lens interface is absent from the literature, and this oversight has been addressed in Chapter 7.

Using a commercial electromagnetic simulation package, the influence of port geometry and substrate parameters on port beam pattern and impedance has been explored. For the first time, the position of the port phase centre has been examined. This discussion provides valuable insight into the behaviour and therefore the design of microstrip and stripline ports.

Replacing the single port model with a linear array of ports, the interplay between ports has been examined. This work focuses on three forms of excitation. The first represents a beam port feed where a single port is excited in the presence of other ports. The second models a beam port constructed using sub-ports, here a small number of ports is excited with a fixed phase and magnitude in the presence of other ports. Finally, the antenna port array is represented by exciting all ports with a fixed magnitude and a variable phase gradient. The results of this analysis demonstrate the need for matching techniques to consider operational environment that each port experiences, not simply the port's physical design.

A matching technique has been developed for each of the three forms of port excitation in Section 7.3. These techniques use the power wave formulation of S-parameters, explained in Section 3.2.4, to examine the performance of the structure when each port is terminated by different loads. Using numerical optimisation and the concept of effective input impedance, the ideal port loads are found. This new method for matching a system where many ports are excited simultaneously also has uses in applications outside the scope of this thesis.

The lens sidewall has long been recognised as an important aspect of a Rotman lens design. Section 7.2.4 describes how the lens sidewall should be shaped to maximise the absorbed energy. This work is supplemented by an analysis of the dummy port matching issues in Section 7.3.3. Further, a novel method of implementing these dummy port loads has been described in Section 7.4.

The insights into port design and matching have been applied to three Rotman lens designs in Section 7.5. The final design achieves a new level in broadband Rotman lens performance. The lens presented in Section 7.5.2 attains a bandwidth of 7 to 20 GHz and a 40° field-of-view. This represents the new state-of-the-art in broadband Rotman lens design.

8.2.3 Limitations of Constrained Lens

The ideal Rotman lens has long been praised for its true time delay properties and therefore its unlimited bandwidth potential. While it is obvious that an infinite bandwidth is not possible, in practice, there is very little understanding of how much bandwidth is achievable from a well designed Rotman lens. This thesis has clearly described the mechanisms that cause aberrations and limit bandwidth, using a broadband monolithic Rotman lens as an example.

The search for the values of the Rotman variables and focal arc which minimise the lens aberrations has occupied much of the work in the literature. Chapter 5 has comprehensively answered these questions for the geometrical performance of the Rotman lens. However, Chapter 7 shows that the aberration levels and bandwidth of the Rotman lens are not strongly influenced by the choice of Rotman variable values. Instead, both the bandwidth and aberration magnitude is dominated by the design and impedance match of the Rotman lens port interface and sidewall.

The first source of phase error in the Rotman lens is the poorly defined phase centre of the microstrip or stripline port. The severity of this problem increases as the field-of-view required to illuminate all the antenna ports increases and the port width increases. Section 7.1.3 shows that this can be improved by calculating the phase centre so that the port can be placed correctly.

The high frequency performance of the Rotman lens is also limited by the higher order modes of each port. While the first order mode can be properly matched, the energy coupling to the second and third port modes will tend to be reflected back into the body of the lens. This causes increased insertion loss and aberrations. While popular practise limits the upper frequency of operation to prevent both second and third order modes from being supported, Section 7.1.2 has demonstrated that the second order mode is not strongly excited in a well designed Rotman lens. This result has increased the upper frequency of operation to prevent the third order mode.

The coupling between beam ports has a fixed magnitude and phase behaviour. This property allows beam ports, single or multi sub-port, to be very well matched. As the effective width of the beam ports is reduced, due to low frequency of operation or compact lens design, the coupling between beam ports becomes stronger. Sections 7.1.4 and 7.2.2 show that reducing the beam port effective width below $\lambda_g/2$ is not practical due to the high insertion loss causes by beam port coupling.

The performance of the antenna ports is strongly affected by inter-port coupling. Unlike beam ports, all antenna ports are excited simultaneously, but with a variable phase gradient. This variable phase gradient prevents the antenna ports from being properly matched for all beam angles. As the lens's field-of-view increases, the quality of the impedance match is diminished. This causes an increasing proportion of the energy to be reflected at the antenna ports, increasing the insertion loss. Section 7.3.2 explains that this effect limits the maximum field-of-view of the lens at the lowest frequency of operation.

Section 7.5.2 describes the design and performance of a broadband Rotman lens. It shows that the Rotman lens is capable of a 4 to 1 bandwidth. However, the design falls short of this limit due to interactions within the beam port feed network. This thesis has not fully addressed this problem, it remains for future work to find a solution.

8.3 Recommended Future Work

This thesis represents a comprehensive study of monolithic Rotman lens design and construction. The remaining gaps in knowledge concern the design and implementation of very broadband, multiple sub-port, beam ports and feed networks. It is this area that reduced the maximum operating bandwidth of the lens demonstrated in Section 7.5.2 to 3:1. In addition, if the beam port phase centre could be better defined by improved design and construction techniques, the high frequency phase performance of the lens may be improved.

Further work on Rotman lens design should focus on new transmission line types. Non-radiating dielectric waveguide could be produced using laser cutting or injection molding techniques. This has the potential to create large lenses that set a new standard of inexpensive beamformers. Innovative port designs may also be used for exciting a propagating wave across the lens from a microstrip or waveguide transmission line.

Surface acoustic waves have been used with great success for filters, oscillators and transformers. These devices may also be used to produce compact low frequency constrained lenses. Such a lens would be constructed using a small plate of piezoelectric substrate and the lens ports would be constructed using specially designed interdigital transducers. This work would require completely new port design and analysis, creating new simulation tools and manufacturing techniques in the area of constrained lens design.

8.4 Summary of Original Contributions

The original contributions in this Thesis that have resulted in a new standard of broadband Rotman lens are discussed in Section 1.2. In summary they include:

1. **Optimal focal arc analysis:** By presenting the Rotman equations normalised to the size of the array aperture, and redefining the phase errors to reflect the lens's intended application of a beam-forming feed network, a thorough analysis of the

optimal focal arc has been conducted. This analysis has shown that aberrations are minimised using a circular focal arc and careful optimisation of the variable g. Refocusing of the focal arc does yield a slight improvement in aberration performance at the optimal value of g. However, the real value of refocusing is that similar aberration levels can be achieved using smaller values of g, and therefore producing a more compact lens.

2. **Symmetrical lens equations and comparison:** By extending the Rotman equations to include the symmetrical lens case, the performance of the symmetrical lens can be compared directly with the classical lens topology. In contrast to claims made in the literature, the symmetrical Rotman lens does not improve aberration performance or reduce lens size.

3. **Characterisation and analysis of the port lens interface:** The port lens interface has been characterised for the first time. This has been used to examine the broadband performance potential of a Rotman lens constructed using microstrip or stripline techniques. This analysis has highlighted the relationship between port geometry and port impedance, higher order modes, phase centre, multi-port interactions, coupling and reflection loss.

4. **Multi-port impedance matching techniques:** The work has demonstrated that the matching technique must be adapted to the form of excitation that each lens port experiences. Single beam ports need only consider the reflected energy, while all other ports must also consider the coupled energy from simultaneously excited ports. This work has made broader bandwidth lenses a possibility.

5. **Broadband lens implementation:** To demonstrate the significance of the theory and methods presented in this thesis, they have been applied to the construction of a 1:4 bandwidth Rotman lens. While a bandwidth of only 3:1 has been achieved, the work demonstrates that 1:4 is possible with some fine tuning of the beam port feed networks. However, a 3:1 bandwidth Rotman lens still represents the current state of the art in constrained lens development.

8.5 In Closing

Constrained lenses, and the Rotman lens in particular, have experienced over forty years of development. In this time, new transmission line technologies have emerged and computers have revolutionised how we simulate and design these devices. This thesis has taken a fresh look at monolithic constrained lens design and applied the latest techniques to gain a new understanding of the capabilities of this old but powerful lens structure. The work presented in this thesis will ensure that the Rotman lens will always present an attractive beam-forming solution.